

JGR Solid Earth

RESEARCH ARTICLE

10.1029/2021JB023641

Key Points:

- The maximum horizontal stress orientation in the upper 3 km varies along the strike of Hikurangi Subduction Margin
- Spatial variation of shallow stress orientations is likely related to along-strike variations in subduction interface coupling behavior
- Variation of stress orientation along depth in the southern Hikurangi margin may reflect low shear stress on the subduction interface

Supporting Information:

Supporting Information may be found in the online version of this article.

Correspondence to:

E. Behboudi,
effat.behboudi@ucdconnect.ie

Citation:

Behboudi, E., McNamara, D. D., Lokmer, I., Wallace, L. M., & Saffer, D. M. (2022). Spatial variation of shallow stress orientation along the Hikurangi Subduction Margin: Insights from in-situ borehole image logging. *Journal of Geophysical Research: Solid Earth*, 127, e2021JB023641. <https://doi.org/10.1029/2021JB023641>

Received 18 NOV 2021

Accepted 5 MAY 2022

Spatial Variation of Shallow Stress Orientation Along the Hikurangi Subduction Margin: Insights From In-Situ Borehole Image Logging

E. Behboudi^{1,2} , D. D. McNamara³ , I. Lokmer^{1,2} , L. M. Wallace^{4,5} , and D. M. Saffer⁵

¹Irish Centre for Applied Geosciences (iCRAG), University College Dublin, Dublin, Republic of Ireland, ²School of Earth Sciences, University College Dublin, Dublin, Republic of Ireland, ³Department of Earth, Ocean and Ecological Sciences, University of Liverpool, Liverpool, UK, ⁴GNS Science, Lower Hutt, New Zealand, ⁵University of Texas Institute for Geophysics, Austin, TX, USA

Abstract Knowledge of the contemporary in-situ stress orientations in the Earth's crust can improve our understanding of active crustal deformation, geodynamic processes, and seismicity in tectonically active regions such as the Hikurangi Subduction Margin (HSM), New Zealand. The HSM subduction interface is characterized by varying slip behavior along strike, which may be a manifestation of combined variations in both stress state and the mechanical properties of faults and their hanging walls. Alternatively, these variations in subduction thrust slip behavior may drive heterogeneity in the stress state in space and time. In this study, we analyze borehole image and oriented four-arm caliper logs acquired from 13 boreholes along the HSM to present a comprehensive stress orientation data set from borehole data within the shallow (<3 km) upper plate of the subduction thrust. Our results reveal a 065°/245° S_{Hmax} orientation within the central HSM (Hawke's Bay region) which rotates to 112°/292° and 140°/320° in the southern HSM. This rotation of S_{Hmax} orientation correlates spatially with along-strike variations in subduction interface slip behavior, characterized by creep and/or shallow episodic slip events in the central HSM and interseismic locking in the south. The borehole S_{Hmax} orientations suggest that contemporary stress orientations may be caused in part by along-strike variation in deformation style imposed by clockwise rotation of forearc. In the southern HSM, borehole-derived S_{Hmax} orientations are inconsistent with S_{Hmax} orientations derived from focal mechanism solutions in the subducting plate, implying some degree of mechanical decoupling between the shallow hanging wall and subducting slab.

Plain Language Summary Movement along faults at tectonic plate boundaries is driven by, and in turn can cause changes in the orientation and magnitude of the stresses in the Earth's crust. Such changes may help to explain tectonic forces that cause faulting and build topography, how earthquakes are generated, and the influence of fluids and rock friction on earthquake occurrence. The Hikurangi Subduction Margin (HSM) is New Zealand's largest and most hazardous plate boundary fault, and exhibits a variety of deformation and earthquake types, which may be linked to concomitant variations in stress orientation. In this study, we found that variability in the stress orientations within the upper plate of HSM corresponds broadly to variations in plate boundary slip behavior, and also reflects observed patterns of contemporary surface deformation. We suggest that these shallow stress orientations encode information about subduction plate interface behavior.

1. Introduction

In-situ stress measurements can provide important insights into stress states at global and localized scales, the geomechanical state of earthquake-hosting faults, shear traction on faults, and processes of stress accumulation and release on plate boundary faults. Such measurements also assist with understanding how crustal stresses relate to strain observed geodetically and geologically (e.g., Brodsky et al., 2017; T. B. Byrne et al., 2009; Magee & Zoback, 1993; Townend & Zoback, 2006; Warren-Smith et al., 2019; Zoback et al., 1987). Earthquake occurrence and many earthquake rupture characteristics are partly dependent on the shear to normal stress ratio, which is a function of the relative magnitude of in-situ principal stresses, the orientation of the fault plane with respect to the principal stresses, pore fluid pressure, and fault plane friction coefficients (Jaeger et al., 2007; Schellart & Rawlinson, 2013; Vavryčuk, 2015). Additionally, earthquakes can redistribute stress, leading to temporal changes in both shear and normal stress on adjacent fault planes and surrounding rocks either statically (a shift in the stress state from before to after the earthquake) or dynamically (oscillating stress changes that occur with the passage of

© 2022. The Authors.

This is an open access article under the terms of the Creative Commons Attribution License, which permits use, distribution and reproduction in any medium, provided the original work is properly cited.

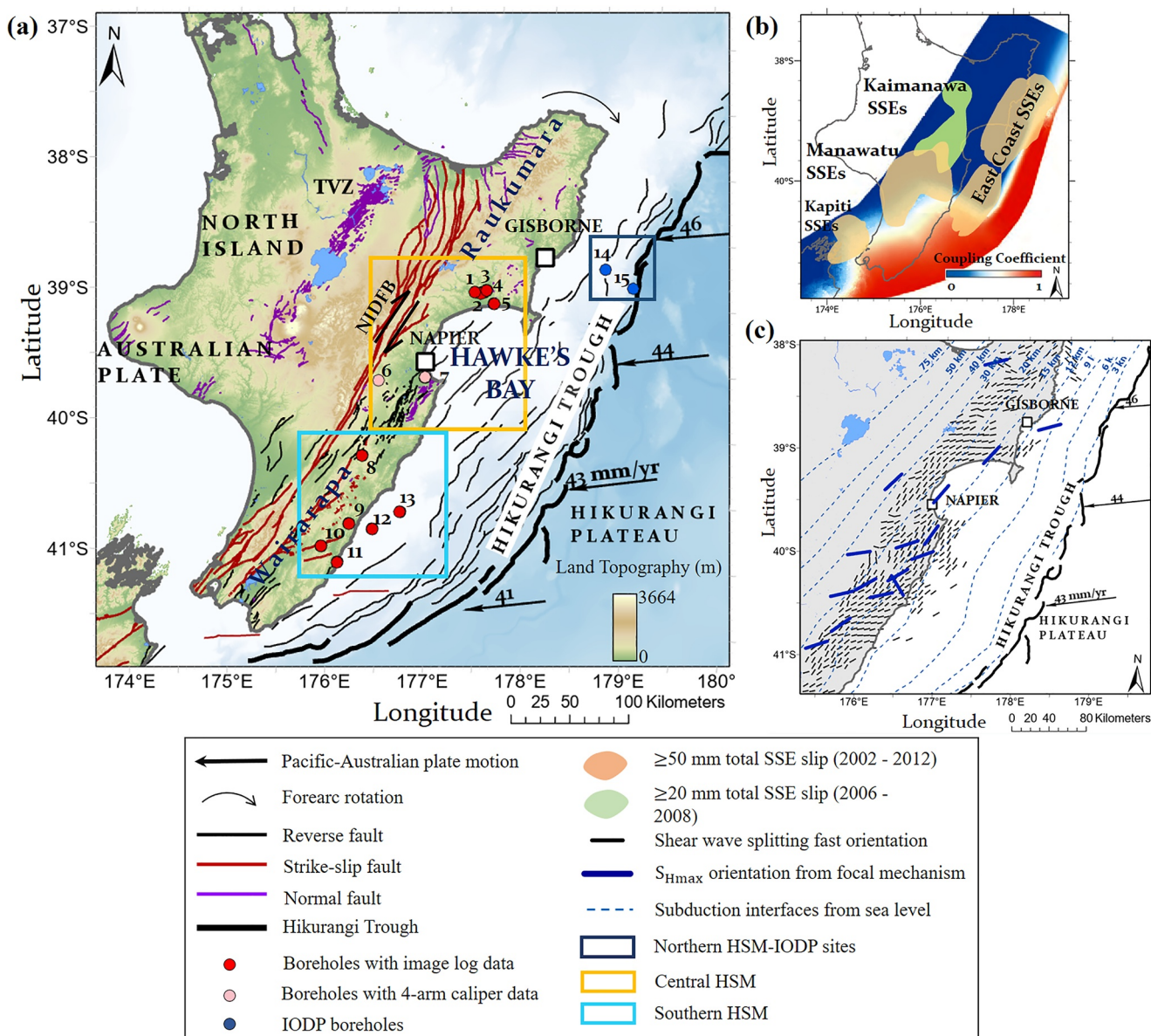


Figure 1. (a) Tectonic setting of East Coast of North Island, New Zealand. Fault traces from Barnes et al. (2010), Langridge et al. (2016), Mountjoy and Barnes (2011), and Pedley et al. (2010). Black arrows indicate the long-term motion between Pacific and Australian plate from Beavan et al. (2002). (b) Interseismic coupling based on campaign GPS velocities (1995–2008), shown in terms of coupling coefficient (Wallace, Beavan, et al., 2012). Orange and green shaded regions represent the cumulative slow slips in 2002 and 2012 (Wallace, Beavan, et al., 2012) and SSEs beneath the Kaimanawa ranges in 2006 and 2008 (Wallace, 2020; Wallace & Eberhart-Phillips, 2013). (c) Map showing $S_{H\max}$ orientations from focal mechanisms (Townend et al., 2012) and shear wave splitting fast orientations (Illsley-Kemp et al., 2019). Boreholes are numbered 1: Makareo-1, 2: Kauhauroa-2, 3: Waitahora-1, 4: Kauhauroa-5, 5: Tuwhāra-1A, 6: Kererū -1, 7: Whakatū-1, 8: Ngapaeruru-1, 9: Te Mai-2, 10: Rauni-2, 11: Orui-1A, 12: Titihaoa-1, 13: Tawatawa-1, 14: U1519A, and 15: U1518B. Abbreviations: NIDFB, North Island Dextral Fault Belt; TVZ, Taupo Volcanic Zone.

seismic waves) (e.g., Brodsky et al., 2017, 2020; Hardebeck, 2004; Hardebeck & Okada, 2018; Ma et al., 2005; Seeber & Armbruster, 2000; Stein, 1999).

The Hikurangi Subduction Margin (HSM), where the Pacific Plate subducts offshore the east coast of the North Island of New Zealand (Figure 1a; Wallace et al., 2004), experiences strong along-strike variations in megathrust slip behavior, ranging from deep interseismic locking (and stress accumulation) beneath the southern North Island, to episodic slow slip events (SSEs) and creep at the northern and central HSM (Figure 1b). Creep and shallow (<15 km depth) SSEs lasting for 2–3 weeks recur every 18–24 months offshore of the northern and

central HSM (Wallace, 2020; Wallace & Beavan, 2010, Figure 1b). Deep (>25 km), long-term (>1 year) slow slip events occur approximately every ~5 years at the southern HSM (Wallace & Beavan, 2010), just down-dip of a portion of the plate interface that is strongly locked and accumulating stress likely to be released in a future great earthquake ($M_w > 8.0$). Despite the recognized importance of in-situ stress states along active subduction zones in understanding strain accumulation and release, few studies have been undertaken to directly measure in-situ stresses or their orientations in these settings (e.g., Brodsky et al., 2017; Chang et al., 2010; Hardebeck, 2015; Huffman et al., 2016; Huffman & Saffer, 2016; Lin et al., 2013, 2016, 2010; Malinverno et al., 2016; McNamara et al., 2021; Saffer et al., 2013; Sibson & Rowland, 2003), particularly where such large along-strike changes in slip behavior occur.

Analysis of earthquake focal mechanism solutions reveals that the maximum horizontal stress (S_{Hmax}) orientations (≤ 60 km depth) are NE-SW in the northern and central HSM and ENE-WSW orientation in the southern HSM (Figure 1c). These stress indicators are largely from earthquakes within the subducting slab, with most located at depths > 25 km (Townend et al., 2012). In contrast, seismic anisotropy fast orientations (which are often assumed to be parallel to S_{Hmax}) determined from shear wave splitting methods that sample the upper ~40 km (Figure 1c) suggest a dominant S_{Hmax} orientation of NE-SW for most of the HSM forearc, while the northern HSM forearc displays variable fast orientations, with a more dominant ENE-WSW inferred S_{Hmax} (Illsley-Kemp et al., 2019).

Shallow (<3 km) S_{Hmax} orientations have been determined from limited analysis of borehole image logs from boreholes drilled onshore and offshore along the HSM (Griffin, 2019; Griffin et al., 2021; Heidbach et al., 2018; Lawrence, 2018; McNamara et al., 2021). Analysis of borehole image data from four onshore boreholes show NE-SW to ENE-WSW S_{Hmax} orientations in the central HSM (Heidbach et al., 2018; Lawrence, 2018), and an E-W to NW-SE S_{Hmax} orientation is determined from three borehole image logs in the southern HSM (Griffin, 2019; Griffin et al., 2021; Heidbach et al., 2018). Boreholes offshore the northern HSM drilled as part of the International Ocean Discovery Program (IODP) Expeditions 372 and 375 show an E-W S_{Hmax} orientation close to the Hikurangi trench, and an NW-SE S_{Hmax} orientation in the offshore forearc (McNamara et al., 2021), indicating strong variations in stress orientations across the forearc.

In this study, we provide a detailed analysis of shallow (<3 km) S_{Hmax} orientations from stress-induced borehole failures, and assess their variability within the upper plate of the HSM. We analyze six borehole image logs and oriented four-arm caliper logs (not previously used for stress orientation studies), and provide a reanalysis of the seven borehole image logs investigated in previous studies (Griffin, 2019; Griffin et al., 2021; Heidbach et al., 2018; Lawrence, 2018), with a focus on acquiring higher resolution measurements (length, width, orientation) of induced borehole failures. We then discuss spatial variations in contemporary S_{Hmax} orientations and their relationship to far-field stresses and long-term patterns of tectonic deformation, and their potential links to along-strike variations in subduction megathrust slip behavior.

2. Geological Setting

The Hikurangi Subduction Margin (HSM) lies along the Pacific-Australian plate boundary at the southern end of the Tonga-Kermadec-Hikurangi Trench, off the east coast of the North Island, New Zealand (Figure 1a). The Hikurangi Subduction Margin accommodates westward subduction of the Hikurangi Plateau (a Cretaceous large igneous province) beneath the continental crust of North Island at the Hikurangi Trough (B. W. Davy, 1992). The Hikurangi Plateau is ~10–15 km thick and transitions to a more typical 5–7 km thick oceanic plate further north at the Kermadec Trench (B. Davy et al., 2008; B. W. Davy, 1992; Ghisetti et al., 2016; Mochizuki et al., 2019). The southern termination of the HSM is located somewhere beneath New Zealand's northeastern South Island, where oblique convergence is transferred to the Marlborough Fault System and Alpine Fault (Barnes et al., 1998; Little & Roberts, 1997).

Neogene to present tectonic deformation across the HSM is complex and includes contributions from shortening associated with subduction at the Hikurangi Trough, clockwise rotation of the East Coast forearc, strike-slip faulting along the North Island Dextral Fault Belt (NIDFB), and back-arc extension in the Taupo Volcanic Zone (TVZ) (Beanland & Haines, 1998; Wallace et al., 2004, Figure 1a). The East Coast forearc has rotated clockwise for at least the last few Myr at the rate of 3°–4°/Myr relative to the Australian plate (Nicol et al., 2007). This rotation results in back-arc rifting in the central North Island's Taupo Volcanic Zone (TVZ), transgression in the southern North Island, and creates a large along-strike change in convergence rate at the Hikurangi

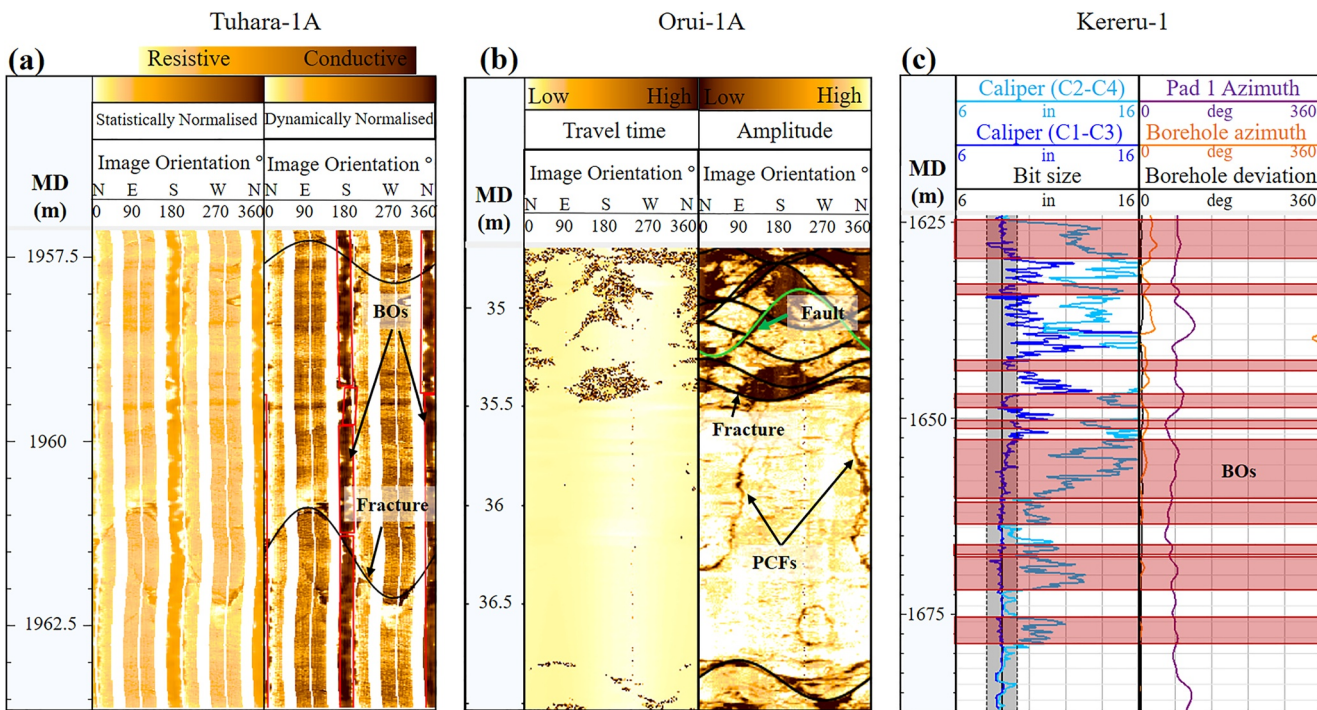


Figure 2. (a) Statistically and dynamically normalized resistivity image log (Fullbore Formation Microimager) showing borehole breakouts and natural fractures in borehole Tuhara-1A, (b) Dynamically normalized travel time and amplitude images from an acoustic image log (Acoustic Formation Imaging Technology) acquired in Orui-1A borehole showing petal centerline fractures, natural fractures, and a fault (observable offset of other geological features across a natural fracture). (c) Plot of an oriented four-arm caliper log (C1-C3 and C2-C4) from borehole Kereru-1. The 10% tolerance of bit size (black line) is shown as a gray shaded zone, plotted next to pad 1 azimuth and borehole orientation information showing caliper enlargement indicative of the presence of a borehole breakout.

Trough, from \sim 20 mm/year in the south to \sim 60 mm/year at the northern Hikurangi Trough (Wallace et al., 2004, Figure 1a). Wallace et al. (2004) suggest that an along-strike change from subduction of the large igneous province (Hikurangi Plateau) at the Hikurangi Trough to normal oceanic crust along the Kermadec Trench exerts a torque on the forearc, producing clockwise rotation of the eastern North Island. Overall, relative motion between the Pacific and Australian plates occurs through this region at \sim 40 mm/yr, and is oblique to the orientation of the plate boundary. The oblique relative motion is partitioned into a margin-perpendicular component and a margin-parallel component. The margin-perpendicular component occurs along the Hikurangi subduction interface and active upper-plate thrust faults within the accretionary wedge and overriding plate (Barnes et al., 1998; Nicol & Beavan, 2003). The margin-parallel component of Pacific-Australia relative plate motion is largely accommodated by a combination of right-lateral strike-slip in the North Island Dextral Fault Belt (NIDFB) and vertical-axis clockwise rotation of the North Island forearc (Beanland & Haines, 1998; Nicol et al., 2007; Wallace et al., 2004).

3. Data and Methodology

We analyze borehole image logs acquired from 11 boreholes using a range of tools including; the Schlumberger Fullbore Formation Microimager (FMITM; Figure 2a) and Oil-Based Mud Imaging tool (OBMITTM), Baker Atlas Simultaneous Acoustic and Resistivity Imager (STARTM), Tiger Energy Services Acoustic Formation Imaging Technology (AFIT; Figure 2b), and two orientated four-arm caliper logs (Figure 2c). The tool types and their borehole wall coverage for each borehole are summarized in Table S1 in Supporting Information S1. Data processing and quality assessment are performed on all image logs, the details of which are documented in the supplementary material (Text S1 and S2 in Supporting Information S1).

From the borehole image logs, we identify stress-induced borehole failures, including borehole breakouts (BOs; Figures 2a and 2c), drilling-induced tensile fractures (DITFs), and petal-centerline fractures (PCFs; Figure 2b). BOs and DITFs are well-known indicators of horizontal in-situ stress orientations in vertical to semi-vertical

boreholes, under the common assumption that one of the principal stresses is vertical stress (S_v). BOs and DITFs develop parallel to the contemporary minimum (S_{hmin}) and maximum (S_{hmax}) horizontal stresses, respectively (Aadnoy & Bell, 1998; Bell, 2003; Bell & Gough, 1979). BOs and DITFs can also be used to determine S_{hmax} orientations in boreholes deviated $\geq 20^\circ$, as long as corrections are applied to address the impact of vertical stress (S_v) on their development (Peška & Zoback, 1995).

BOs form as enlargements of the borehole diameter on opposite sides of the borehole wall where the circumferential hoop stress, induced by non-uniform horizontal principal stress magnitudes, is large enough to exceed the rock strength (Bell & Gough, 1979; Zoback, 2007). Borehole breakouts typically appear on resistivity image logs as a pair of wide, out-of-focus zones, conductive (in water-based mud; Figure 2a) or resistive (in oil-based mud, such as OBMI tool; King et al., 2010) zones. In acoustic televiewer logs, they appear as low amplitude and long travel time zones. In both types of logs, BOs are located $\sim 180^\circ$ from each other around the circumference of the borehole wall. BOs often correlate with borehole enlargement and are associated with large caliper values as the result of the borehole failure (Figure 2c; Tingay et al., 2016). In this study we use these criteria to identify BOs from available image logs, only identifying features as BOs if there are two present at the same depth interval and they are oriented $180^\circ \pm 10^\circ$ from each other around the borehole circumference.

Oriented four-arm caliper data are also used to infer the presence of BOs along boreholes. To reliably distinguish BOs from other non-stress related enlargements, such as keyseats and washouts, we apply the criteria presented by Reinecker et al. (2016). They recommend that all four-arm caliper data, borehole deviation and azimuth, and pad 1 azimuth must be controlled carefully to interpret borehole breakouts. The following criteria are considered: (a) one pair of caliper arms reads very close to the bit size while the opposite pair measures a larger diameter; (b) caliper differences must exceed the bit size by 10%; (c) rotation of the tool ceases in breakout zones; and (d) the enlargement zone must extend more than one meter vertically.

DITFs develop on the borehole wall where there is a significant difference between the two horizontal principal stress magnitudes and the local stress concentrations around the borehole wall lead to hoop stresses that overcome the tensile strength of the rock (C. Barton et al., 2009; Brudy & Zoback, 1999; Zoback, 2007). DITFs typically appear as narrow, conductive (on resistivity image logs) or low amplitude and longer travel time (on acoustic image logs) pairs, $\sim 180^\circ$ from each other around the circumference of the borehole wall. DITFs are generally parallel or slightly inclined to the borehole axis in vertical to semi-vertical boreholes (C. A. Barton et al., 1998; Bell, 2003; Rajabi et al., 2016a, 2016b; Tingay et al., 2016). In this study, DITF selection criteria follows these considerations and only accepts pairs of DITFs located within the same depth interval that are $180^\circ \pm 10^\circ$ from each other around the borehole circumference.

Here, all BOs and DITFs are reported as individual feature lengths and widths, such that a single BO or DITF measurement does not span a number of separate individual BOs or DITFs, similar to what has been done in previously analyzed image logs along the HSM (Griffin, 2019; Lawrence, 2018). This is an important aspect of quantifying induced features from borehole image logs because geological properties, such as varying strength associated with variably bedded lithologies, impact the development and growth (both width and length) of borehole breakouts (Fellgett et al., 2019; Kingdon et al., 2016). It is also important to capture each induced feature individually for accurate statistical considerations of borehole stress orientations.

PCFs are induced fractures that form within the bedrock ahead of the drill bit in response to stress concentrations at the bottom of the borehole during drilling and propagate inward toward the borehole (Davatzes & Hickman, 2010; Y. Li & Schmitt, 1998; Wenning et al., 2017). PCFs appear as conductive (resistivity image logs) or low amplitude (acoustic image logs) partial sinusoids that merge into discontinuous borehole axial centerline fractures (Figure 2b, Kulander et al., 1990). The average of the centerline fracture orientations or dip orientation of the partial sinusoids of a PCF is parallel to the orientation of S_{hmin} (Davatzes & Hickman, 2010). In contrast to the DITFs, the centerline portions of PCFs are often less than 180° from each other around the circumference of the borehole wall. We identify PCFs when the entire structure (petal fracture and both centerline fractures) are visible on the image log, and where the centerline fractures do not fall into the criteria used for identifying DITFs ($180^\circ \pm 10^\circ$).

The quantitative World Stress Map (WSM) quality ranking system (where A-quality data is a reliable indicator of regional stress orientations and E-quality is more likely representative of localized stress orientation) and circular statistical analysis is used here to provide quantified uncertainty for all reported stress orientations from borehole

Table 1

Stress Indicators From Analysis of Borehole Image Logs and Oriented Four-Arm Caliper Data in the Central HSM, New Zealand

Borehole ID	Latitude (DD)	Longitude (DD)	Max borehole deviation (°)	Total depth (m MD)	Image interval (m MD)	Feature type	Number	Mean S _{Hmax} (°)	S.D. (°)	Total length (m)	Quality
Kauhauroa-2	-38.962592	177.407183	1.78	2138.5	1824.2–2138.5	BO	52	069°/249°	15	24	C
Kauhauroa-5	-38.936292	177.463518	2.57	1754.4	1277.1–1754.4	BO	260	052°/232°	16	75	B
						DITF	1	020°/195°	—	3.1	D
Makareo-1	-38.953047	177.348347	2.65	942.4	484.7–942.4	BO	140	058°/238°	20	60	B
Tuhara-1A	-39.035152	177.544434	7.64	2276.9	1708–2151.2	BO	334	071°/251°	15	239	B
Kereru-1	-39.659492	176.43688	1	1938	1622–1920	BO	16	079°/259°	14	43	C
Whakatu-1	-39.620447	176.896152	1.53	1455	525–1400	BO	8	144°/324°	11	13	D

Note. Mean S_{Hmax} azimuths, standard deviations (S.D.), and data quality ranking are calculated according to World Stress Map conventions (Heidbach et al., 2016). Latitude and longitude are reported in decimal degrees (DD).

image and oriented four-arm caliper logs (e.g., Heidbach et al., 2016). A detailed explanation of these calculations can be found in the supplementary material (Text S3 in Supporting Information S1). Borehole locations, image log intervals, mean S_{Hmax} orientation, standard deviation, and WSM quality classification based on the length-weighted method (Heidbach et al., 2016) for individual boreholes are summarized in Table 1 and Table 2.

4. Results

4.1. Central HSM (Hawke's Bay Region)

A total of 810 BOs with a combined length of 454 m are identified from borehole image and oriented four-arm caliper logs acquired in Kauhauroa-2, Kauhauroa-5, Makareo-1, Tuhara-1A, Kereru-1, and Whakatu-1 boreholes in the Central HSM region (Table 1; see Figure 1 for the borehole locations and names). Using only BOs from boreholes with B-C quality rankings (following the WSM criteria), and so more likely to represent far-field stress orientations, a dominant 155°/335° ± 10° orientation is observed, indicating a 155°/335° ± 10° (NW-SE) S_{hmin} orientation, from which we infer an S_{Hmax} orientation of 065°/245° ± 10° (ENE-WSW) (Figure 3). The only exception is borehole Whakatu-1 (WSM D quality ranking), in the southeast area of the central HSM, which shows a dominant BO orientation of 054°/234° ± 13° (NE-SW), from which we infer a 144°/324° ± 13° (NW-SE) S_{Hmax} orientation (Table 1; Figure 3). One DITF pair is observed in borehole Kauhauroa-5 with a mean

Table 2

Stress Indicators From Analysis of Borehole Image Logs in the Southern HSM, New Zealand

Borehole ID	Latitude (DD)	Longitude (DD)	Max borehole deviation (°)	Total depth (m MD)	Image interval (m MD)	Feature type	Number	Mean S _{Hmax} (°)	S.D. (°)	Total length (m)	Quality
Ngapaeruru-1	-40.24199	176.2999	11.2–17.78	1418.5	941.8–1418.5	BO	282	112°/292°	12	62	B
Ranui-2a	-40.942317	175.917819	8.1–25.4	1440.7	839–1130	BO	390	94°/274°	17	51	B
					1130–1422.5	BO		145°/325°	16	49	B
Te Mai-2	-40.765984	176.194344	2.4	193.1	35–147.5	BO	2	109°/289°	8	0.5	D
Orui-1A	-41.065181	176.087846	1.6	117.3	6.7–114.5	BO	4	155°/335°	11	0.4	D
						PCF	1	125°	—	0.8	C
						DITF	1	133°/295°	—	0.2	D
Titihaoa-1	-40.799708	176.430936	2.3	2745.6	1983–2745.6	BO	14	152°/332°	10	7	D
Tawatawa-1	-40.659736	176.698303	2.9	1560	749–1539.2	BO	825	103°/283°	14	350	B

Note. Mean S_{Hmax} azimuths, standard deviations (S.D.), and data quality ranking are calculated according to World Stress Map conventions (Heidbach et al., 2016). Latitude and longitude are reported in decimal degrees (DD).

^aMeasured stress feature orientations are not corrected for borehole deviations ≥20°.

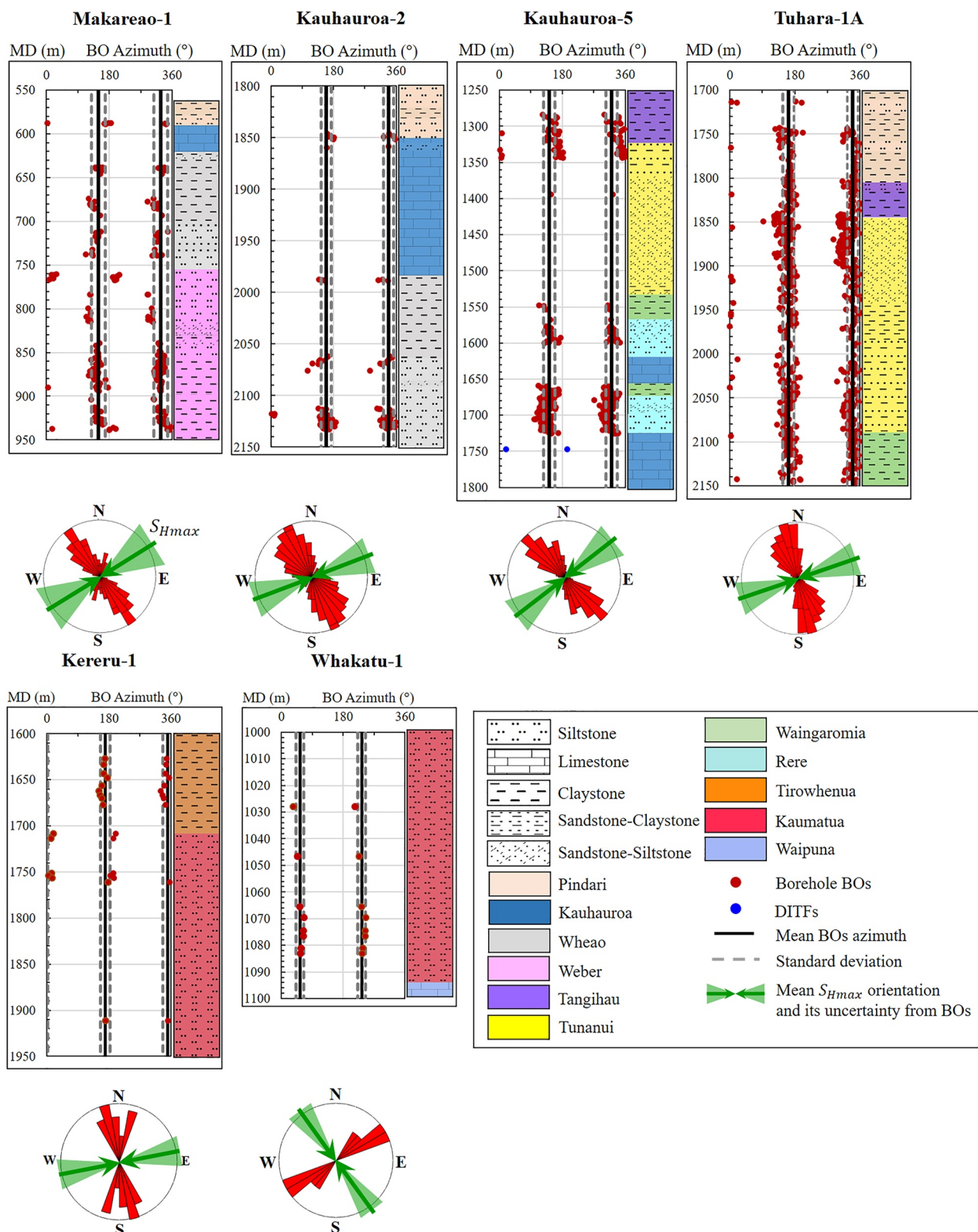


Figure 3. Graph of breakout (BO) azimuths (red dots), drilling-induced tensile fractures azimuths (blue dots), and stratigraphy column against measured depth (m MD) for boreholes at the central Hikurangi Subduction Margin. Mean BO azimuths and the standard deviation for individual borehole are plotted in black and dashed gray lines respectively. Bi-directional rose diagram of breakout and $S_{H\max}$ orientations for each borehole is shown below BO panels.

$S_{H\max}$ orientation of $020^\circ/195^\circ$ (NNE-SSW) (Figure 3). No BOs, DITFs, or PCFs are observed in Waitahora-1 borehole from OBMI image log (this image log only provided $\sim 37\%$ coverage of borehole wall) or from oriented four-arm caliper data.

4.2. Southern HSM

A total of 1517 BOs with a combined length of 520 m are identified from borehole image logs in boreholes Ngapaeruru-1, Rauni-2, Titihaoa-1, Tawatawa-1, Te Mai-2, and Orui-1A (Table 2; see Figure 1 for the borehole locations and names). For borehole stress data with a WSM quality ranking of B (Ngapaeruru-1, Tawatawa-1, and Ranui-2) we observe an $S_{h\min}$ orientation of $022^\circ/202^\circ \pm 20^\circ$ from which we infer an $S_{H\max}$ orientation of $112^\circ/292^\circ \pm 20^\circ$ (WNW-ESE) (Figure 4). An $S_{H\max}$ orientation of $140^\circ/320^\circ \pm 22^\circ$ (NW-SE) is observed from D-quality data (Table 2; Figure 4). Our reanalysis of BOs from borehole Ranui-2 suggests a 51° clockwise $S_{H\max}$ orientation rotation from E-W ($094^\circ/274^\circ \pm 17^\circ$) in the shallower imaged depth interval (842–1130 m MD) to NW-SE ($145^\circ/325^\circ \pm 16^\circ$) in the deeper imaged interval (1130–1422 m MD) (Table 2; Figure 4) that was first reported by Griffin (2019).

5. Discussion

5.1. Spatial Variation of Shallow $S_{H\max}$ Orientations

Our results show that contemporary $S_{H\max}$ orientations in the HSM upper plate change from $065^\circ/245^\circ \pm 10^\circ$ (ENE-WSW) along the central HSM to $112^\circ/292^\circ \pm 20^\circ$ (WNW-ESE) in the southern HSM (with a local $S_{H\max}$ orientation of $140^\circ/320^\circ \pm 22^\circ$ (NW-SE) from D-quality data) (Figure 5). The $065^\circ/245^\circ \pm 10^\circ$ borehole-derived $S_{H\max}$ orientation in the central HSM is rotated modestly ($\sim 17^\circ$) anticlockwise with respect to the Pacific-Australian plate motion (82° ; Beavan et al., 2002). This implies that far-field plate boundary forces exerted at the HSM may be the primary control on the contemporary stress orientations within the upper plate in this region. In contrast, the $112^\circ/292^\circ \pm 20^\circ$ borehole-derived $S_{H\max}$ orientation in the southern HSM is rotated $\sim 30^\circ$ clockwise (bearing $\sim 58^\circ$ rotation from localized D-quality $140^\circ/320^\circ \pm 22^\circ$ $S_{H\max}$ orientations) relative to the Pacific-Australian plate motion (Figure 5). This observed 47° – 75° along-strike rotation in $S_{H\max}$ orientation may result from a number of possible influences, including (a) along-strike variations in subduction interface coupling behavior, (b) HSM forearc kinematics and long-term tectonic deformation, (c) lateral variations in basement topography along strike, or (d) regional changes in recent slips on local active faults, surface topography, and geomechanical stratigraphy along strike.

The spatial pattern of rotation in borehole-derived $S_{H\max}$ orientations along the HSM is consistent with the location of changes in subduction interface coupling from north to south (Figures 1b and 5). In the northern and central HSM, the subduction interface is largely creeping and experiences shallow (< 15 km), episodic slow slip events that extend offshore and possibly to the trench. At the southern HSM the plate interface is strongly interseismically coupled to ~ 30 km depth, and is currently accumulating elastic strain in the surrounding crust (e.g., Wallace, 2020, Figure 1b). Accrual of elastic compressional strain and stress resulted from interseismic coupling in the southern HSM could impose a NW-SE component (parallel to the convergence direction between the Hikurangi forearc and subducting plate) to the approximately E-W Pacific-Australian plate motion. This may result in the observed WNW-ESE $S_{H\max}$ orientation ($112^\circ/292^\circ$ – $140^\circ/320^\circ$) in the shallow upper plate.

The HSM experiences a dominantly compressional tectonic regime due to subduction; however rapid clockwise rotation of the forearc, which accommodates the margin-parallel component of oblique Pacific-Australian plate motion, results in significant tectonic transitions along strike (Nicol et al., 2007; Wallace et al., 2004). Deformation resulting from clockwise rotation of the Hikurangi forearc drives strike-slip and/or normal faulting within the onshore portion of the northern and central HSM, and transpressional faulting in the southern HSM (Figure 5, Fagereng & Ellis, 2009; Nicol et al., 2007; Wallace et al., 2004; Wallace, Fagereng, & Ellis, 2012). This variation in upper plate tectonic deformation along the HSM strike may explain our observed along-strike variation in $S_{H\max}$ orientations. If the NE-SW and/or ENE-WSW striking faults in the central HSM are strike-slip to normal faults, then the NE-SW $S_{H\max}$ orientation in the central HSM may reflect margin-normal extension. Similarly, WNW-ESE/NW-SE $S_{H\max}$ orientations are consistent with reverse to transpressional NE-SW/ENE-WSW striking faults in the southern HSM. Variation in tectonic deformation due to oblique plate convergence has been suggested

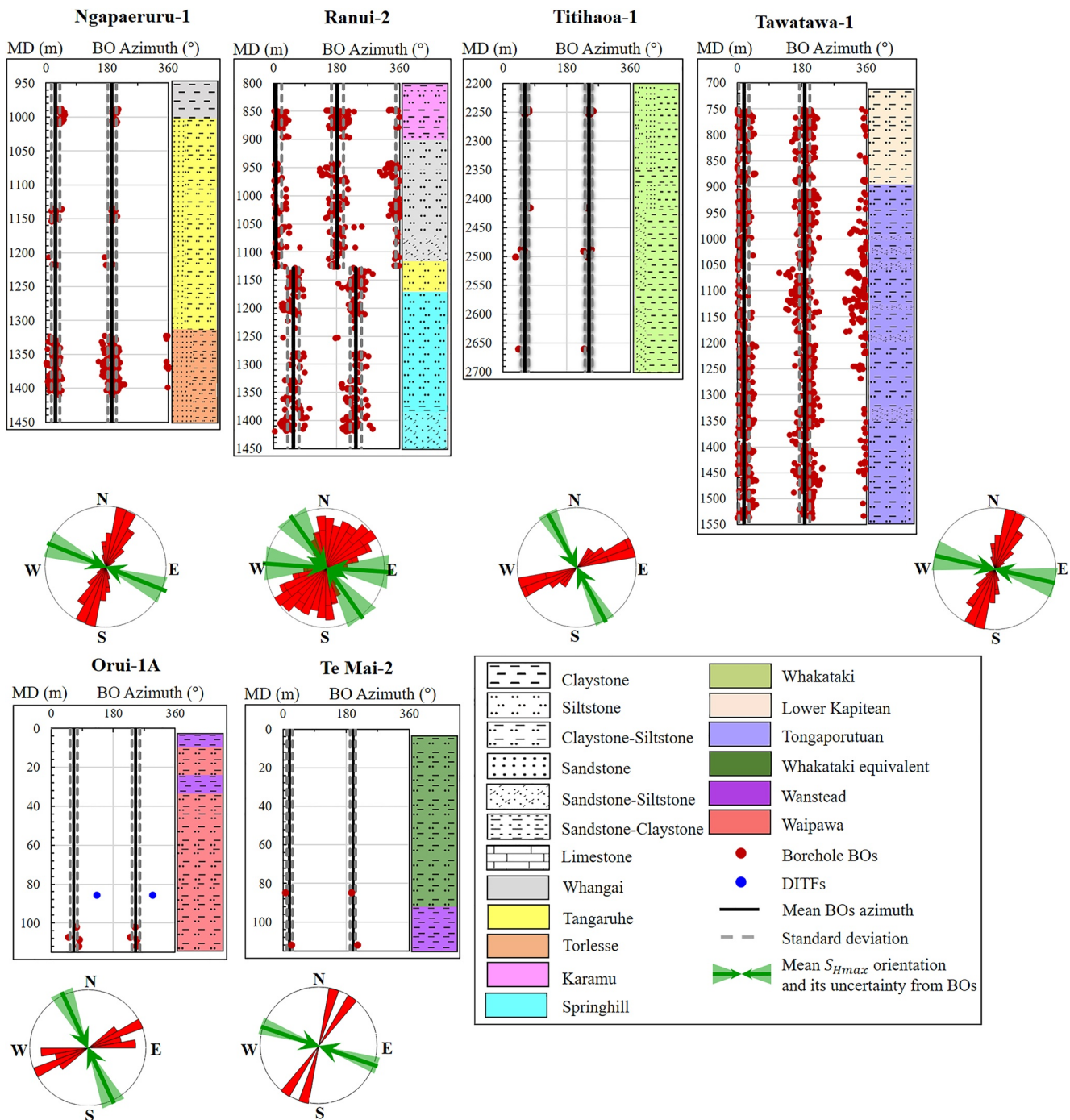
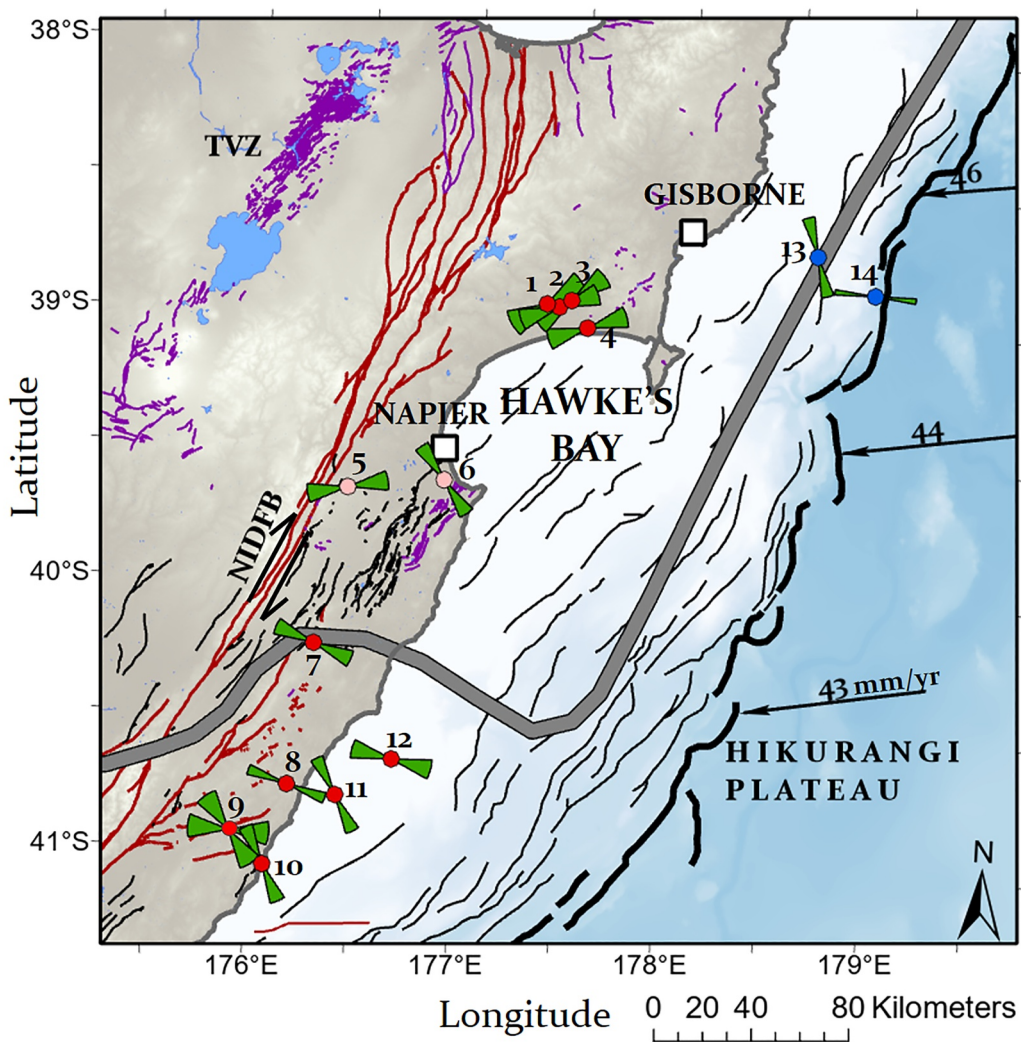


Figure 4. Graph of breakout (BO) azimuths (red dots), drilling-induced tensile fractures azimuths (blue dots), and stratigraphy column against measured depth (m MD) for boreholes at the southern Hikurangi Subduction Margin. Mean BO azimuths and the standard deviation for individual borehole are plotted in black and dashed gray lines respectively. Bi-directional rose diagram of breakout and S_{Hmax} orientations for each borehole is shown below BO panels.

to explain S_{Hmax} orientation variations in the Nankai subduction zone (Chang et al., 2010; Lin et al., 2010; Tobin et al., 2009; Wu et al., 2012) and the Costa Rica margin (Malinverno et al., 2016).

Basement topographic variation, such as uplifted basement blocks or seamounts, can introduce gravity and density changes within the crust creating geomechanical inhomogeneities (e.g., Bassett et al., 2022; Chow et al., 2022). Such geomechanical inhomogeneities can add horizontal compressional stress around the uplifted basement margins and extensional stress above them, changing the stress orientations (Artyushkov, 1973; Bott, 1991;



	$S_{H\max}$ orientation from BOs	1: Makareo-1	8: Te Mai-2
	The boundary between low- and high-interseismic coupling on the subduction interface	2: Kauhauroa-2	9: Rauni-2
	Hikurangi Trough	3: Kauhauroa-5	10: Orui-1A
	Pacific-Australian plate motion	4: Tuahura-1A	11: Titihaoa-1
	Reverse fault	5: Kereru -1	12: Tawatawa-1
	Strike-slip fault	6: Whakatu-1	13: U1519A
	Normal fault	7: Ngapaeruru-1	14: U1518B
	Boreholes with image log data	● IODP boreholes	
	Boreholes with oriented 4-arm caliper logs		

Figure 5. Map of $S_{H\max}$ at the East Coast of North Island determined from borehole breakouts (green bowties). International Ocean Discovery Program borehole-derived $S_{H\max}$ orientations are from McNamara et al. (2021). Active faults traces from Barnes et al. (2010), Langridge et al. (2016), Litchfield et al. (2014), Mountjoy and Barnes (2011), and Pedley et al. (2010). The bold black line shows the Hikurangi Trough. Black arrows indicate the relative convergence vector between the Pacific and Australian Plates from Beavan et al. (2002). Abbreviations: NIDFB, North Island Dextral Fault Belt; TVZ, Taupo Volcanic Zone.

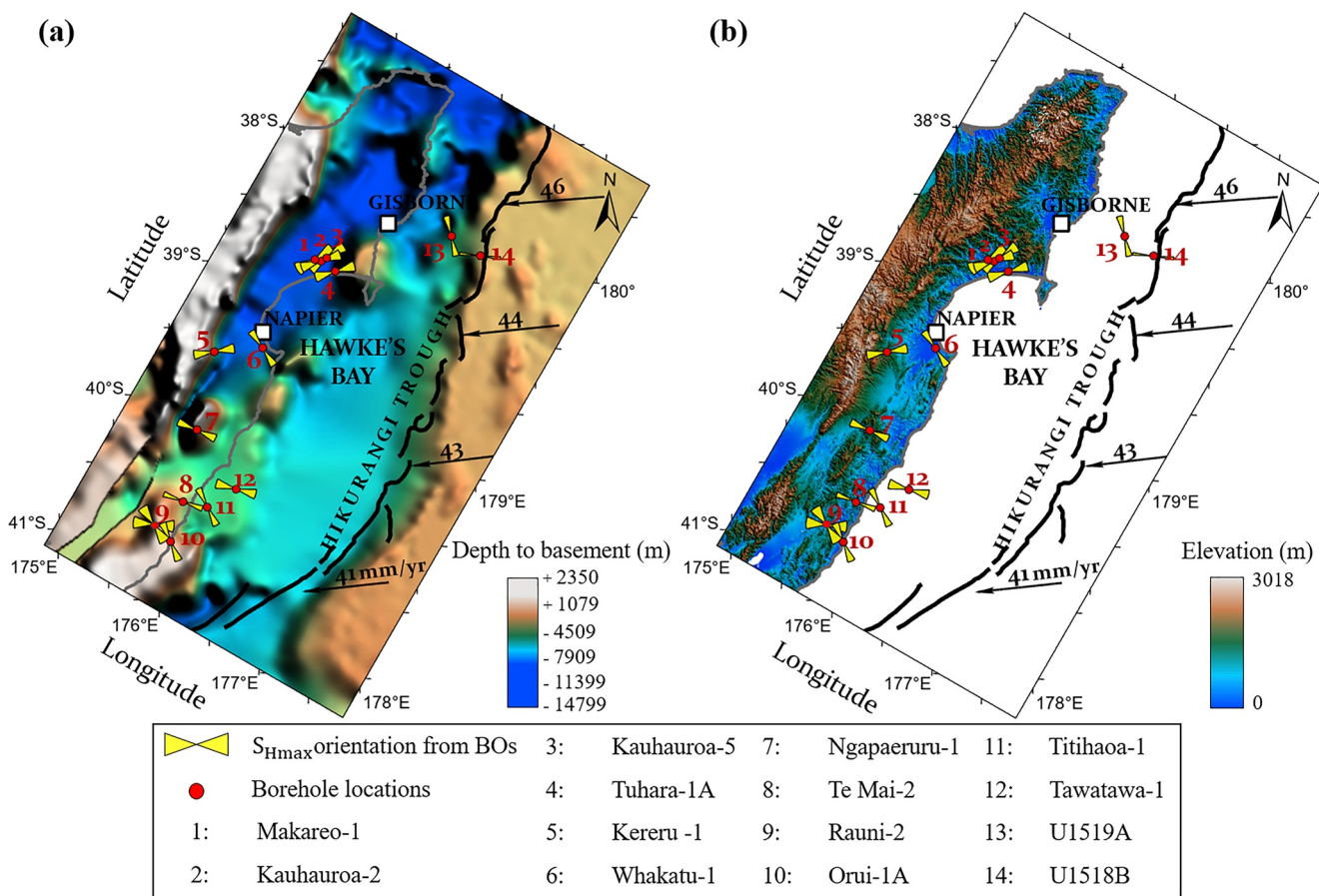


Figure 6. (a) Map showing depth to basement of North Island adapted from FROGTECH (2013), and borehole-derived $S_{H\max}$ orientations (yellow bowties). $S_{H\max}$ orientation is rotated in front of the basement uplift in the central Hikurangi Subduction Margin. Black arrows indicate the long-term motion between Pacific and Australian Plates from Beavan et al. (2002). (b) Map showing digital elevation model (FROGTECH, 2013) which indicates the elevation of neotectonic and active geological structures.

Enever et al., 1999; Gale et al., 1984; Rajabi et al., 2016a; Ruh et al., 2016; Sun et al., 2020). This may partly produce our observed $S_{H\max}$ rotation. For example, the SEEBASE™ depth to basement model of New Zealand (Figure 6a; FROGTECH, 2013) shows that the central HSM basement is deeper (~9–15 km) than the southern HSM basement (<5 km) (Figure 6a). Most southern HSM borehole-derived $S_{H\max}$ orientation measurements are located on basement topographic highs while the central HSM measurements are located in areas where the basement is deep. Furthermore, localized basement highs can be observed within the central HSM (Figure 6a). Two of the central HSM borehole-derived $S_{H\max}$ measurements (boreholes 4 and 5 in Figure 6a) are located close to the margins of these basement highs and as such their orientation may be influenced by them. However, as these $S_{H\max}$ orientations align with other measurements made away from these basement topographic features, we consider this to be unlikely.

Linked to the central to southern change in basement topography are surface topography (Figure 6b) and geomechanical heterogeneities introduced by variations in rock and sediment physical properties, both of which can influence $S_{H\max}$ orientations. The variable basement topography means surface topography is more pronounced in the southern HSM than the central HSM (Figure 6b). This may influence $S_{H\max}$ orientations in shallow depth intervals (<500 m below sea level) such as boreholes Te Mai-2 and Orui-1A (boreholes 8 and 10 in Figure 6b). However, given that the borehole breakouts used to measure $S_{H\max}$ orientations from this region are mostly located at depths 600–2700 m below sea level, we infer that surface topography is not a primary factor controlling the observed $S_{H\max}$ rotation. Finally, due to basement uplift in the southern HSM, borehole breakouts are measured in a wider variety of lithologies (Miocene to Cretaceous sediments) than in the northern HSM (dominantly Miocene sediments). If the wider ranges of lithologies in the southern HSM are geomechanically

different from those in the central HSM, this lateral heterogeneity in mechanical rock properties could in part be responsible for the $S_{H\max}$ rotation.

Recent slips on active faults are also known to reorient stress, creating variations in $S_{H\max}$ orientations both along the region and with depth (e.g., D. Li et al., 2018; Provost & Houston, 2001; Rice, 1992). However, it cannot feasibly explain the large-scale $S_{H\max}$ orientation rotation observed along the HSM strike, beyond what has already been discussed with respect to deformation style changing from strike-slip/normal faulting in the central HSM, to the dominantly reverse and transpressional faulting in the southern HSM. However, recent faulting may explain some of the localized $S_{H\max}$ rotations observed within the central and southern HSM regions. For instance, at borehole Whakatu-1 (boreholes 6 in Figure 5) a $144^\circ/324^\circ \pm 11^\circ$ (NW-SE) $S_{H\max}$ orientation is noted, which is rotated $\sim 80^\circ$ from the dominant $065^\circ/245^\circ \pm 10^\circ$ $S_{H\max}$ orientation in the central HSM (Figure 5). The NW-SE $S_{H\max}$ orientation in Whakatu-1 is perpendicular to the HSM margin and to observed active, NNE-SSW striking reverse faults in this region (Figure 5, Hull, 1987; Langridge et al., 2016; Litchfield et al., 2014). Similarly, Griffin (2019) suggests the activity of nearby faults as the cause of the observed $S_{H\max}$ rotation along depth in borehole Ranui-2.

5.2. Shallow $S_{H\max}$ Orientations and Maximum Contraction Directions

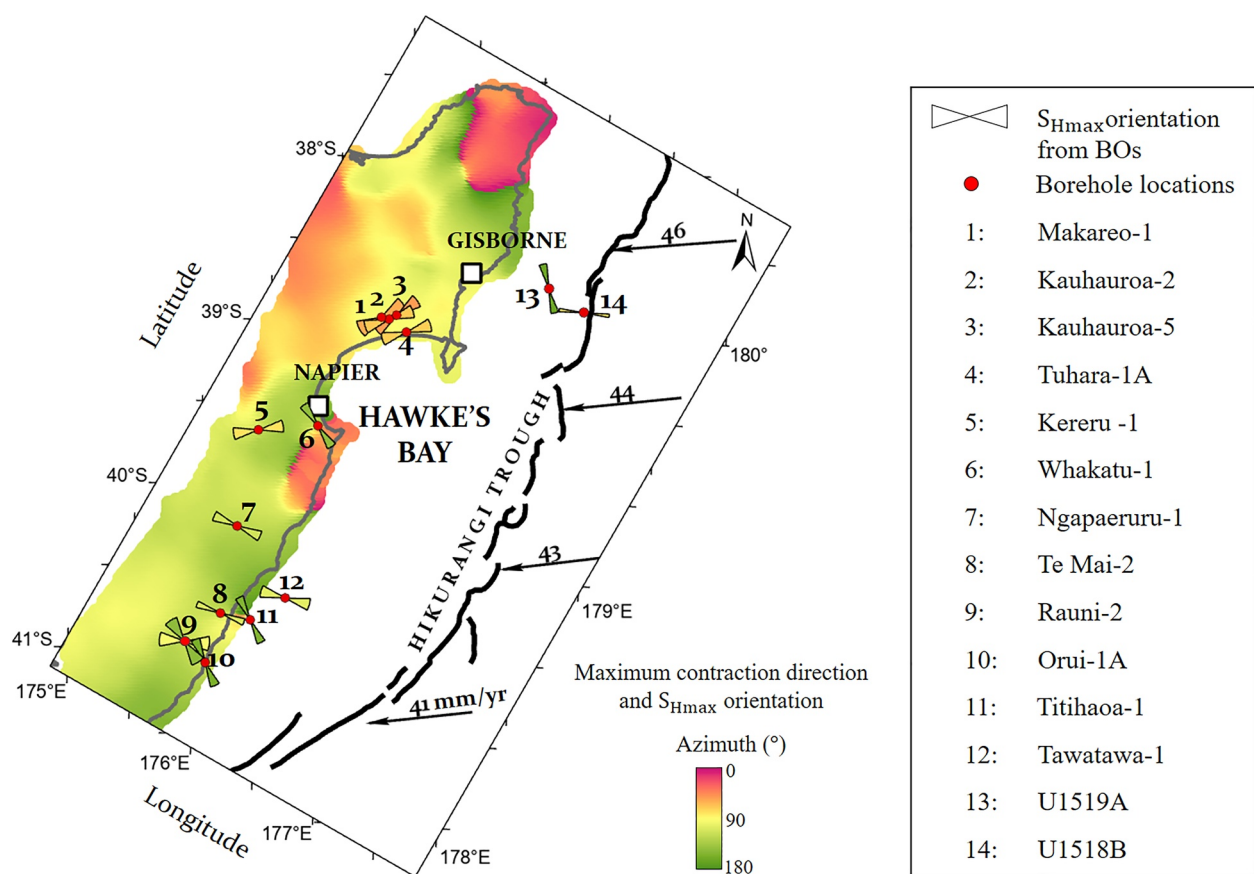
Geodetic measurements over the last 25 years have been used to determine New Zealand's contemporary surface strain field (Dimitrova et al., 2016; Haines & Wallace, 2020). Maximum contraction directions change from dominantly E-W in the northern central HSM (Hawke's Bay region), to a mix of both NE-SW and WNW-ESE in the southern central HSM, to WNW-ESE and NW-SE directions in the southern HSM (Figure 7a, Haines & Wallace, 2020). The majority of $S_{H\max}$ orientations are within 40° of GPS maximum contraction directions (Figure 7b), indicating that the two datasets are broadly compatible, although there is one outlier with a misalignment of $\sim 57^\circ$ (borehole 6 in Figure 7b). The broad agreement between shallow $S_{H\max}$ orientations and geodetic maximum contraction directions may suggest that stress orientations in the upper plate are influenced by elastic strain arising from interseismic coupling on the Hikurangi subduction interface.

The observed variable misalignment of maximum contraction directions and $S_{H\max}$ orientations (Figure 7b) may reflect variations in the shallow $S_{H\max}$ orientations (as explained in 5.1) or temporal changes in stress orientation at the HSM. This is unlikely for the HSM as the borehole data and GPS measurements were collected within the same time period, 1994–2013 and 1995–2013, respectively. Similar widespread stress-strain direction misalignment is also noted at the Nankai and Cascadia subduction zones (e.g., Townend & Zoback, 2006; Wang, 2000; Wang et al., 1995). Wang (2000) explains the misalignment of maximum contraction directions with respect to $S_{H\max}$ as a result of geodetic strain signals reflecting temporal changes in the stress state associated with the subduction earthquake cycle. Townend and Zoback (2006) explained this mismatch in SW Japan by showing that the stress orientations determined from focal mechanisms within the upper plate are more strongly influenced by long-term tectonic processes (convergence between northeastern Honshu and Amuria plate), while the geodetic strain orientations are dominated by interseismic strain accumulation between large earthquakes. This could certainly be the case at HSM, although observed differences between stress orientations and maximum contraction directions are not as dissimilar as those reported for the SW Japan case, making it difficult to disentangle the influence of long-term plate motion versus earthquake cycle processes on the HSM upper plate stress field.

5.3. Variation of $S_{H\max}$ Orientations With Depth

Townend et al. (2012) derived $S_{H\max}$ orientations from earthquake focal mechanisms (≤ 60 km depth) between 2004 and 2011, and observed an average $S_{H\max}$ orientation of $060^\circ/240^\circ \pm 17^\circ$ for the central HSM, and $066^\circ/246^\circ \pm 22^\circ$ for the southern HSM (Figure 8a; calculation of average $S_{H\max}$ orientation is explained in supplementary material (Text S3 in Supporting Information S1)). Comparing focal mechanism-derived to borehole-derived $S_{H\max}$ orientations shows that in the central HSM they are closely aligned (borehole: $065^\circ/245^\circ \pm 10^\circ$; focal mechanism: $60^\circ/240^\circ \pm 17^\circ$). In contrast, the southern HSM shows an apparent stress field rotation of 46° – 74° with depth (borehole $S_{H\max}$: $112^\circ/292^\circ \pm 20^\circ$ – $140^\circ/320^\circ \pm 22^\circ$; focal mechanism $S_{H\max}$ $66^\circ/246^\circ \pm 22^\circ$) (Figure 8b). Only one compressional focal mechanism $S_{H\max}$ orientation ($149^\circ/329^\circ \pm 33^\circ$) in the southern HSM (latitude 40.5°S), located at ~ 25 km depth (near the subduction interface), aligns with the borehole-derived $S_{H\max}$ orientations for the southern HSM ($112^\circ/292^\circ \pm 20^\circ$ – $140^\circ/320^\circ \pm 22^\circ$) (Figures 8a and 8b).

(a)



(b)

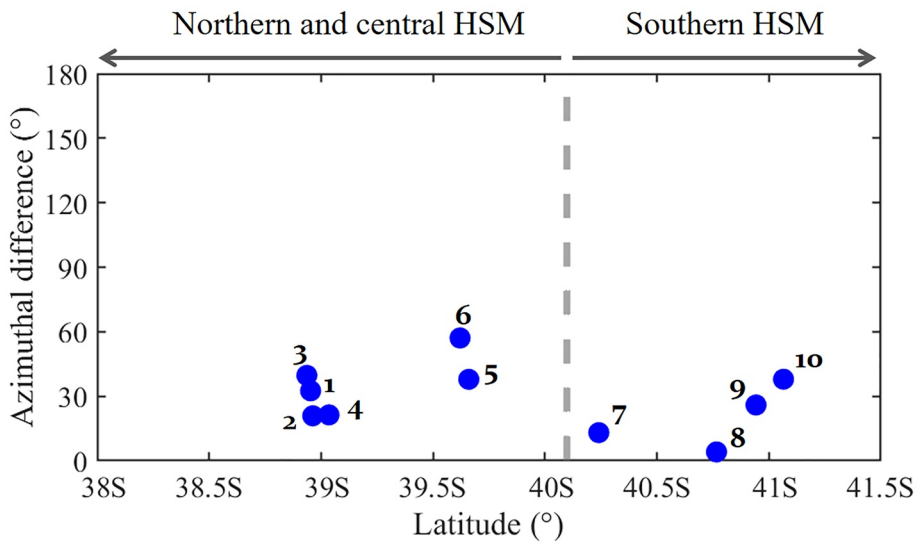
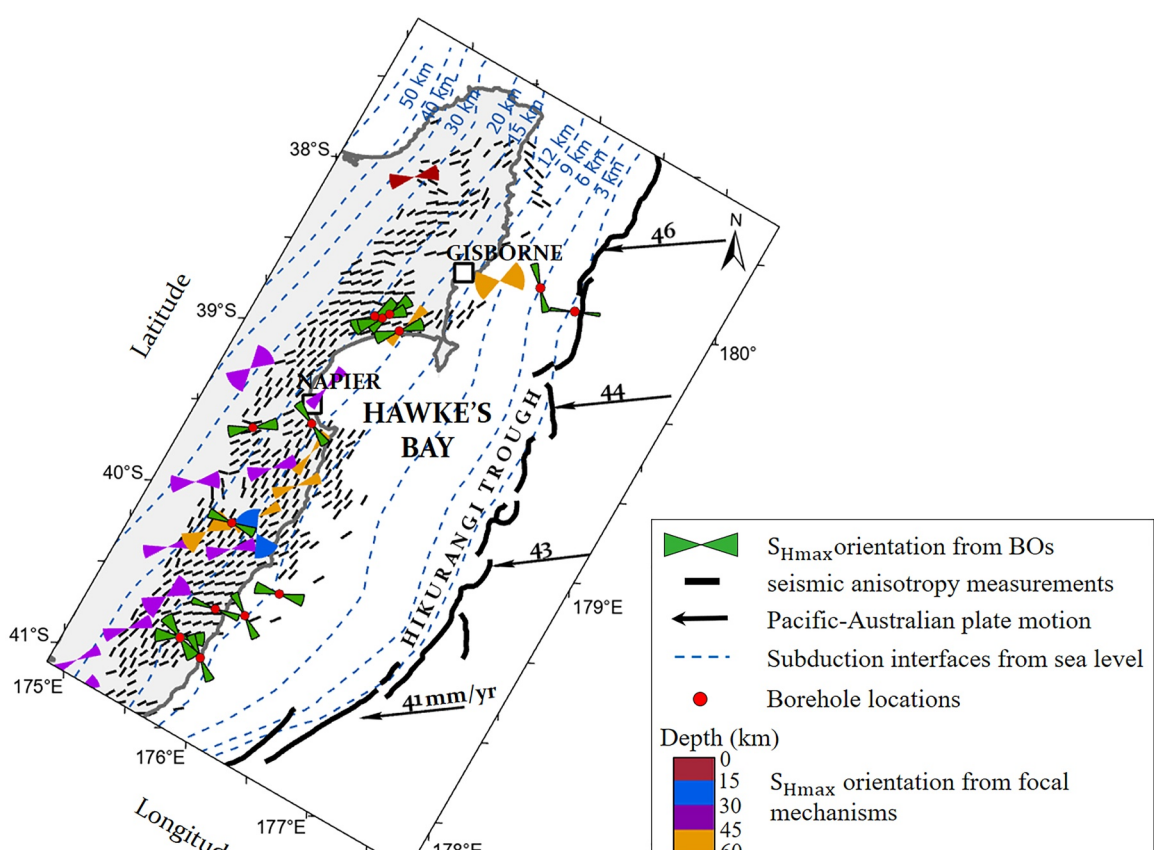


Figure 7. (a) Map of maximum contraction directions from GPS data (Haines & Wallace, 2020) and borehole-derived S_{Hmax} orientations. International Ocean Discovery Program borehole-derived S_{Hmax} orientations are from McNamara et al. (2021). (b) Absolute azimuthal difference between maximum contraction directions and borehole-derived S_{Hmax} orientations at borehole locations.

Stress rotations with depth can be generated by a number of mechanisms, including (a) topography, (b) shallow fault activity, and (c) mechanical anisotropy or heterogeneity. Topography is ruled out as the majority of borehole breakouts come from depths deeper than the amplitude of local topography. Active faulting in the shallow crust has been used to explain S_{Hmax} orientation rotation with depth at the borehole scale in the southern HSM

(a)



(b)

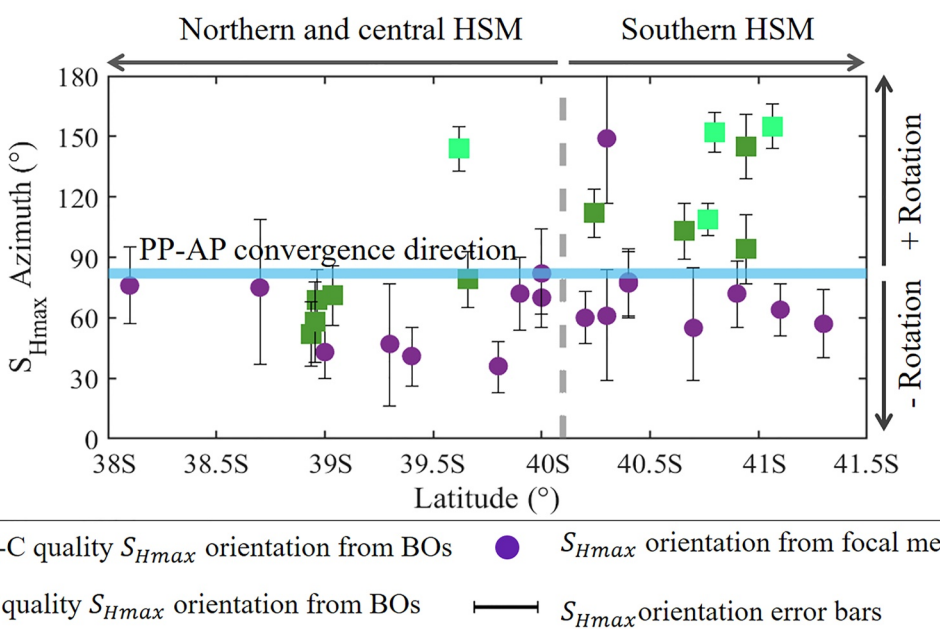


Figure 8. (a) Map of $S_{H\max}$ orientations from focal mechanisms (0–60 km; Townend et al., 2012), seismic anisotropy measurements from shear wave splitting (0–40 km; Illsley-Kemp et al., 2019), and borehole-derived $S_{H\max}$ orientations (green bowties). International Ocean Discovery Program borehole-derived $S_{H\max}$ orientations are from McNamara et al. (2021). Dashed blue lines show depth of subduction interface from sea level (Williams et al., 2013). (b) The graph showing variation of borehole-derived $S_{H\max}$ orientations with respect to Pacific-Australian plate (PP-AP) motion along Hikurangi Subduction Margin (HSM) strike and with depth in the southern HSM.

(Ranui-2; Griffin, 2019). Faults in the region are both reverse and strike-slip, and predominantly striking NE-SW to ENE-WSW (Langridge et al., 2016; Litchfield et al., 2014). Slip on these shallow reverse faults may rotate the $S_{H\max}$ into the observed NW-SE orientations recorded from borehole data here, while the overall subduction $S_{H\max}$ at depth remains in a NE-SW orientation driven by relative plate motion. High fluid pressure can also encourage slip on deeper faults, although in the southern HSM, magnetotelluric data (Heise et al., 2019), seismic tomography studies (Bassett et al., 2014; Eberhart-Phillips et al., 2017), and borehole analysis (except for offshore boreholes Titiahoa-1 and Tawatawa-1; Burgreen-Chan et al., 2016; Darby & Funnell, 2001) do not provide evidence for elevated fluid content or pressure.

Considering borehole-derived WNW-ESE/NW-SE $S_{H\max}$ orientations and focal-mechanism derived NW-SE $S_{H\max}$ orientation, located at ~ 25 km depth, the rotation in the $S_{H\max}$ orientation may occur across the plate interface. In this case, the hanging wall would be mechanically decoupled from the subducting plate, generating the observed rotation in $S_{H\max}$ above (from borehole data) and below it (from focal mechanism data). Such decoupling may imply a low shear stress on the plate interface. Mechanical decoupling has been suggested to occur on subduction plate interfaces elsewhere, though these findings often show principal stresses changing from vertical to horizontal, not a rotation in the horizontal stress orientation as observed here (T. Byrne & Fisher, 1990; Flemings & Saffer, 2018). Further information on the likely strength of the plate interface is required to investigate this theory. Linking the idea of weak faults creating geomechanical heterogeneities and the activity of shallow faults together may provide a further explanation for the shallow $S_{H\max}$ in the southern HSM.

More recently, Illsley-Kemp et al. (2019) measured seismic anisotropy using shear wave splitting fast orientations from earthquake data based on the assumption that they align to $S_{H\max}$ orientation if other significant crustal anisotropies are not present (e.g., fracturing, faulting, grain, and crustal preferred orientations) (Araragi et al., 2015; Boness & Zoback, 2006; Johnson et al., 2011; Pastori et al., 2019; Yang et al., 2011; Zinke & Zoback, 2000). Illsley-Kemp et al. (2019) report a dominant NE-SW (030° – 060°) $S_{H\max}$ orientation for the Hikurangi forearc, with some areas showing a more ENE-WSW orientation (060° – 090°), such as the Hawke's Bay area. In comparison to borehole-derived $S_{H\max}$ orientations presented here (Figure 8a), the two datasets agree in the central HSM shallow crust but not in the southern HSM, with a NE-SW shear-wave splitting and a borehole-derived $S_{H\max}$ of NW-SE. Illsley-Kemp et al. (2019) report that their data is generated from a depth range of 0–40 km which at the Hikurangi forearc captures the upper plate, the plate interface, and the subducting plate. The discrepancy between the two $S_{H\max}$ orientations is thus likely due to (a) the shear wave splitting-derived data are sampling the subducting plate stress field, which seems likely as those directions broadly match focal-mechanisms subducting plate $S_{H\max}$ orientation (Figure 8a), (b) the borehole-derived $S_{H\max}$ orientations are only consistent for the upper few km of the upper plate crust, or (c) the fast directions are controlled by NE-SW striking faulting in the region, which is suggested to be the case by Illsley-Kemp et al. (2019) or other crustal anisotropies.

6. Conclusions

This paper presents a comprehensive analysis of contemporary $S_{H\max}$ orientations from borehole data along the HSM, and discusses stress field orientation variability within the context of variable tectonics and slip behavior of this subduction margin. $S_{H\max}$ orientations in the central HSM are predominately $065^{\circ}/245^{\circ}$, which rotates to a dominantly $112^{\circ}/292^{\circ} \pm 20^{\circ}$ $S_{H\max}$ orientation in the southern HSM. Our borehole-derived $S_{H\max}$ orientations vary along the HSM suggesting that the observed stress orientations are likely caused by along-strike variation in interseismic coupling behavior of the Hikurangi subduction interface. The long-term tectonic deformation arising from rapid rotation of the Hikurangi forearc, causing reverse faulting and strike-slip in the southern part of the margin and a combination of extension and strike-slip in the northern and central margin, may in part cause the along-strike variations in observed stress orientations. The basement uplifts may also be at play in influencing the along-strike variations in observed stress orientations by imposing a horizontal compressional stress component near the uplifted margin, introducing surface topography and geomechanical heterogeneities. However, the extent to which basement topography may change $S_{H\max}$ orientation along the HSM requires further data and modeling. $S_{H\max}$ orientations measured from boreholes are mostly within 40° of maximum contraction directions, suggesting that the observed stress orientations could be influenced by elastic strain arising from interseismic coupling on the subduction interface. In the southern HSM, borehole-derived $S_{H\max}$ orientations are 46° – 74° to $S_{H\max}$ orientations derived from focal mechanism solutions in the subducting plate, implying that the shallow upper plate is mechanically decoupled from the slab, potentially reflecting low shear strength along the plate

interface. Further interpretation of HSM stress state could be achieved by constraining stress magnitudes, which will be the focus of future studies.

Data Availability Statement

This research used data provided by the New Zealand Petroleum and Minerals group (NZPM) within the Ministry for Business, Innovation and Employment (MBIE). The borehole image logs and oriented four-arm caliper data used in this paper can accessed through MBIE's online free database (<https://data.nzpm.govt.nz/GOLD/system/mainframe.asp>). All additional data used in this article were collected from published sources referenced in the text. Borehole breakout measurements presented in this study can be accessed at https://github.com/BehboudiEffatGeo/StressCharacterization_HSM.git and <https://doi.org/10.5281/zenodo.6402741> (Behboudi et al., 2022).

Acknowledgments

This publication has emanated from research conducted with the financial support of Science Foundation Ireland (SFI) under Grant Nos. 17/RC-PhD/3481 and co-funded by the Geological Survey of Ireland (GSI). We appreciate the Editor Isabelle Manighetti, John Townend, Associate Editor, and an anonymous reviewer for constructive and insightful reviews which have greatly improved the manuscript. The authors would like to thank the New Zealand Petroleum and Minerals group (NZPM) within the Ministry for Business, Innovation and Employment (MBIE) for providing access to borehole data and supporting materials for this study. We also thank Schlumberger for providing academic licenses for Techlog 2018.1 to University College Dublin and University of Liverpool. We thank Esri for providing the academic license of ArcGIS Pro to University College Dublin. For the purpose of Open Access, the author has applied a CC BY public copyright license to any Author Accepted Manuscript version arising from this submission. Open access funding provided by IReL.

References

- Aadnoy, B. S., & Bell, J. S. (1998). Classification of drill-induce fractures and their relationship to in-situ stress directions. *Log Analyst*, 39(06), 27–42.
- Araragi, K. R., Savage, M. K., Ohminato, T., & Aoki, Y. (2015). Seismic anisotropy of the upper crust around Mount Fuji, Japan. *Journal of Geophysical Research: Solid Earth*, 120, 2739–2751. <https://doi.org/10.1002/2014JB011554>
- Artყyushkov, E. V. (1973). Stresses in the lithosphere caused by crustal thickness inhomogeneities. *Journal of Geophysical Research*, 78(32), 7675–7708. <https://doi.org/10.1029/jb078i032p07675>
- Barnes, P. M., Lamarche, G., Bialas, J., Henrys, S., Pecher, I., Netzeband, G. L., et al. (2010). Tectonic and geological framework for gas hydrates and cold seeps on the Hikurangi Subduction Margin, New Zealand. *Marine Geology*, 272(1–4), 26–48. <https://doi.org/10.1016/j.margeo.2009.03.012>
- Barnes, P. M., Lpinay, M. D., Collot, J. Y., Delteil, J., & Audru, J.-C. (1998). Strain partitioning in the transition area between oblique subduction and continental collision, Hikurangi margin. *Tectonics*, 17(4), 534–557. <https://doi.org/10.1029/98tc00974>
- Barton, C., Moos, D., & Tezuka, K. (2009). Geomechanical wellbore imaging : Implications for reservoir fracture permeability. *American Association of Petroleum Geologists Bulletin*, 93(11), 1551–1569. <https://doi.org/10.1306/06180909030>
- Barton, C. A., Hickman, S., Morin, R., Zoback, M. D., & Benoit, D. (1998). Reservoir-scale fracture permeability in the Dixie Valley, Nevada, geothermal field. *SPE/ISRM Rock Mechanics in Petroleum Engineering*, Trondheim, Norway, 47371, 315–322. <https://doi.org/10.2118/47371-ms>
- Bassett, D., Arnulf, A., Henrys, S., Barker, D., van Avendonk, H., Bangs, N., et al. (2022). Crustal structure of the Hikurangi margin from SHIRE seismic data and the relationship between forearc structure and shallow megathrust slip behavior. *Geophysical Research Letters*, 49, e2021GL096960. <https://doi.org/10.1029/2021GL096960>
- Bassett, D., Sutherland, R., & Henrys, S. (2014). Slow wavespeeds and fluid overpressure in a region of shallow geodetic locking and slow slip, Hikurangi subduction margin, New Zealand. *Earth and Planetary Science Letters*, 389, 1–13. <https://doi.org/10.1016/j.epsl.2013.12.021>
- Beanland, S., & Haines, J. (1998). The kinematics of active deformation in the North Island, New Zealand, determined from geological strain rates. *New Zealand Journal of Geology and Geophysics*, 41(4), 311–323. <https://doi.org/10.1080/00288306.1998.9514813>
- Beavan, J., Tregoning, P., Bevis, M., Kato, T., & Meertens, C. (2002). Motion and rigidity of the Pacific Plate and implications for plate boundary deformation. *Journal of Geophysical Research*, 107(B10). ETG-19. <https://doi.org/10.1029/2001jb000282>
- Behboudi, E., McNamara, D. D., Lokmer, I., Wallace, L. M., & Saffer, D. M. (2022). Spatial variation of shallow stress orientation along the Hikurangi Subduction Margin: Insights from in-situ borehole image logging [Dataset]. Zenodo. <https://doi.org/10.5281/zenodo.6402741>
- Bell, J. S. (2003). Practical methods for estimating in situ stresses for borehole stability applications in sedimentary basins. *Journal of Petroleum Science and Engineering*, 38(3–4), 111–119. [https://doi.org/10.1016/S0920-4105\(03\)00025-1](https://doi.org/10.1016/S0920-4105(03)00025-1)
- Bell, J. S., & Gough, D. I. (1979). Northeast-southwest compressive stress in Alberta evidence from oil wells. *Earth and Planetary Science Letters*, 45(2), 475–482. [https://doi.org/10.1016/0012-821X\(79\)90146-8](https://doi.org/10.1016/0012-821X(79)90146-8)
- Boness, N. L., & Zoback, M. D. (2006). Mapping stress and structurally controlled crustal shear velocity anisotropy in California. *Geology*, 34(10), 825–828. <https://doi.org/10.1130/G22309.1>
- Bott, M. (1991). Ridge push and associated plate interior stress in normal and hot spot regions. *Tectonophysics*, 200(1–3), 17–32. [https://doi.org/10.1016/0040-1951\(91\)90003-B](https://doi.org/10.1016/0040-1951(91)90003-B)
- Brodsky, E. E., Mori, J. J., Anderson, L., Chester, F. M., Conin, M., Dunham, E. M., et al. (2020). The state of stress on the fault before, during, and after a major earthquake. *Annual review of Earth and planetary sciences*, 48(May). <https://doi.org/10.1146/annurev-earth-053018-060507>
- Brodsky, E. E., Saffer, D., Fulton, P., Chester, F., Conin, M., Huffman, K., et al. (2017). The postearthquake stress state on the Tohoku megathrust as constrained by reanalysis of the JFAST breakout data. *Geophysical Research Letters*, 44, 8294–8302. <https://doi.org/10.1002/2017GL074027>
- Brudy, M., & Zoback, M. D. (1999). Drilling-induced tensile wall-fractures: Implications for determination of in-situ stress orientation and magnitude. *International Journal of Rock Mechanics and Mining Sciences*, 36(2), 191–215. [https://doi.org/10.1016/S0148-9062\(98\)00182-X](https://doi.org/10.1016/S0148-9062(98)00182-X)
- Burgreen-Chan, B., Meisling, K. E., & Graham, S. (2016). Basin and petroleum system modeling of the East Coast basin, New Zealand: A test of overpressure scenarios in a convergent margin. *Basin Research*, 28(4), 536–567. <https://doi.org/10.1111/bre.12121>
- Byrne, T., & Fisher, D. (1990). Evidence for a weak and overpressured décollement beneath sediment-dominated accretionary prisms. *Journal of Geophysical Research*, 95(B6), 9081–9097. <https://doi.org/10.1029/jb095ib06p09081>
- Byrne, T. B., Lin, W., Tsutsumi, A., Yamamoto, Y., Lewis, J. C., Kanagawa, K., et al. (2009). Anelastic strain recovery reveals extension across SW Japan subduction zone Anelastic strain recovery reveals extension across SW Japan subduction zone. *Geophysical Research Letters*, 36(23), L23310. <https://doi.org/10.1029/2009GL040749>
- Chang, C., McNeill, L. C., Moore, J. C., Lin, W., Conin, M., & Yamada, Y. (2010). In situ stress state in the Nankai accretionary wedge estimated from borehole wall failures. *Geochemistry, Geophysics, Geosystems*, 11(12), 1–17. <https://doi.org/10.1029/2010GC003261>
- Chow, B., Kaneko, Y., & Townend, J. (2022). Evidence for deeply subducted lower-plate seamounts at the Hikurangi Subduction Margin: Implications for seismic and aseismic behavior. *Journal of Geophysical Research: Solid Earth*, 127, e2021JB022866. <https://doi.org/10.1029/2021JB022866>

- Darby, D., & Funnell, R. H. (2001). Overpressure associated with a convergent plate margin: East Coast basin, New Zealand. *Petroleum Geoscience*, 7(3), 291–299. <https://doi.org/10.1144/petgeo.7.3.291>
- Davatzes, N. C., & Hickman, S. H. (2010). Stress, fracture, and fluid-flow analysis using acoustic and electrical image logs in hot fractured granites of the Coso geothermal field, California, U.S.A. In M. Po'ppelreiter, C. Garcí'a-Carballido, & M. Kraaijveld (Eds.), *Dipmeter and borehole image log technology* (Vol. 92, pp. 259–293). American Association of Petroleum Geologists Memoir. <https://doi.org/10.1306/13181288M923134>
- Davy, B., Hoernle, K., & Werner, R. (2008). Hikurangi Plateau: Crustal structure, rifted formation, and Gondwana subduction history. *Geochemistry, Geophysics, Geosystems*, 9(7), Q07004. <https://doi.org/10.1029/2007GC001855>
- Davy, B. W. (1992). The influence of subducting plate buoyancy on subduction of the Hikurangi-Chatham Plateau beneath the North Island, New Zealand. *Geology and geophysics of continental margins*.
- Dimitrova, L. L., Wallace, L. M., Haines, A. J., & Williams, C. A. (2016). High-resolution view of active tectonic deformation along the Hikurangi subduction margin and the Taupo Volcanic Zone, New Zealand. *New Zealand Journal of Geology and Geophysics*, 59(1), 43–57. <https://doi.org/10.1080/00288306.2015.1127823>
- Eberhart-Phillips, D., Bannister, S., & Reyners, M. (2017). Deciphering the 3-D distribution of fluid along the shallow Hikurangi subduction zone using P- and S-wave attenuation. *Geophysical Journal International*, 211(2), 1032–1045. <https://doi.org/10.1093/gji/ggx348>
- Enever, J. R., Gale, W., & Fabjanczuk, M. (1999). *A study of the variability of the horizontal stress field in a sedimentary basin* (pp. 1257–1260). 9th International Society for Rock Mechanics Congress.
- Fagereng, A., & Ellis, S. (2009). On factors controlling the depth of interseismic coupling on the Hikurangi subduction interface, New Zealand. *Earth and Planetary Science Letters*, 278, 120–130. <https://doi.org/10.1016/j.epsl.2008.11.033>
- Fellgett, M. W., Kingdon, A., Waters, C. N., Field, L., Shreeve, J., Dobbs, M., & Ougier-simonin, A. (2019). Lithological constraints on bore-hole wall failure ; a study on the Pennine coal measures of the United Kingdom. *Frontiers of Earth Science*, 7(163). <https://doi.org/10.3389-feart.2019.00163>
- Flemings, P. B., & Saffer, D. M. (2018). Pressure and stress prediction in the Nankai accretionary prism: A critical state soil mechanics porosity-based approach. *Journal of Geophysical Research: Solid Earth*, 123, 1089–1115. <https://doi.org/10.1002/2017JB015025>
- FROGTECH. (2013). *New Zealand extended continental shelf SEEBASE™ project*. Report prepared for the Government of New Zealand, Department of Petroleum and Minerals.
- Gale, W. J., Enever, J. R., Blackwood, R. L., & McKay, J. (1984). *An Investigation of the Effect of a Fault/monocline Structure on the In-Situ Stress Field and Mining Conditions at Nattai Bulli Colliery NSW, Australia* (Vol. 48). CSIRO Australia, Division of Geomechanics. Geomechanics of Coal Mining Report No.
- Ghisetti, F. C., Barnes, P. M., Ellis, S., Plaza-Faverola, A. A., & Barker, D. H. N. (2016). The last 2 Myr of accretionary wedge construction in the central Hikurangi margin (North Island, New Zealand): Insights from structural modeling. *Geochemistry, Geophysics, Geosystems*, 17(11), 4517–4533. <https://doi.org/10.1002/2016GC006341>
- Griffin, A. G. (2019). Subsurface S_{Hmax} determined from a borehole image log, onshore southern East Coast Basin, New Zealand. *New Zealand Journal of Geology and Geophysics*, 62(2), 273–290. <https://doi.org/10.1080/00288306.2019.1570946>
- Griffin, A. G., Bland, K. J., Morgans, H. E. G., & Strogen, D. P. (2021). A multifaceted study of the offshore Titihaoa-1 drillhole and a Neogene accretionary slope basin , Hikurangi subduction margin. *New Zealand Journal of Geology and Geophysics*. <https://doi.org/10.1080/00288306.2021.1932527>
- Haines, A. J., & Wallace, L. M. (2020). New Zealand-wide geodetic strain rates using a physics-based approach. *Geophysical Research Letters*, 47(1), e2019GL084606. <https://doi.org/10.1029/2019GL084606>
- Hardebeck, J. L. (2004). Stress triggering and earthquake probability estimates. *Journal of Geophysical Research*, 109(B4), B04310. <https://doi.org/10.1029/2003JB002437>
- Hardebeck, J. L. (2015). Stress orientations in subduction zones and the strength of subduction megathrust faults. *Science*, 349(6253), 1213–1216. <https://doi.org/10.1126/science.aac5625>
- Hardebeck, J. L., & Okada, T. (2018). Temporal stress changes caused by earthquakes: A review. *Journal of Geophysical Research: Solid Earth*, 123, 1350–1365. <https://doi.org/10.1002/2017JB014617>
- Heidbach, O., Barth, A., Müller, B., Reinecker, J., Stephansson, O., Tingay, M., & Zang, A. (2016). WSM quality ranking scheme, database description and analysis guidelines for stress indicator. In *World Stress Map Technical Report 16-01*. GFZ German Research Centre for Geosciences. <https://doi.org/10.2312/wsm.2016.001>
- Heidbach, O., Rajabi, M., Cui, X., Fuchs, K., Müller, B., Reinecker, J., et al. (2018). The world stress map database release 2016: Crustal stress pattern across scales. *Tectonophysics*, 744, 484–98. <https://doi.org/10.1016/j.tecto.2018.07.007>
- Heise, W., Ogawa, Y., Bertrand, E. A., Caldwell, T. G., Yoshimura, R., Ichihara, H., et al. (2019). Electrical resistivity imaging of the interplate coupling transition at the Hikurangi subduction margin, New Zealand. *Earth and Planetary Science Letters*, 524, 115710. <https://doi.org/10.1016/j.epsl.2019.115710>
- Huffman, K. A., & Saffer, D. M. (2016). In situ stress magnitudes at the toe of the Nankai Trough Accretionary Prism, offshore Shikoku Island, Japan. *Journal of Geophysical Research: Solid Earth*, 121, 1202–1217. <https://doi.org/10.1002/2015JB012415>
- Huffman, K. A., Saffer, D. M., & Dugan, B. (2016). In situ stress magnitude and rock strength in the Nankai accretionary complex: A novel approach using paired constraints from downhole data in two wells 4. *Seismology, Earth Planets and Space*, 68(1), 1–9. <https://doi.org/10.1186/s40623-016-0491-4>
- Hull, A. (1987). A late holocene marine terrace on the kidnappers coast, North Island, New Zealand: Some implications for shore platform development processes and uplift mechanism. *Quaternary Research*, 28(2), 183–195. [https://doi.org/10.1016/0033-5894\(87\)90058-5](https://doi.org/10.1016/0033-5894(87)90058-5)
- Illsley-Kemp, F., Savage, M. K., Wilson, C. J. N., & Bannister, S. (2019). Mapping stress and structure from subducting slab to magmatic rift: Crustal seismic anisotropy of the North Island, New Zealand. *Geochemistry, Geophysics, Geosystems*, 20, 5038–5056. <https://doi.org/10.1029/2019gc008529>
- Jaeger, J., Cook, N., & Zimmerman, R. (2007). *Fundamentals of rock mechanics*. Wiley-Blackwell.
- Johnson, J. H., Savage, M. K., & Townend, J. (2011). Distinguishing between stress-induced and structural anisotropy at Mount Ruapehu Volcano, New Zealand. *Journal of Geophysical Research*, 116(B12), B12303. <https://doi.org/10.1029/2011JB008308>
- King, R. C., Tingay, M. R. P., Hillis, R. R., Morley, C. K., & Clark, J. (2010). Present-day stress orientations and tectonic provinces of the NW Borneo collisional margin. *Journal of Geophysical Research*, 115(10), B10415. <https://doi.org/10.1029/2009JB006997>
- Kingdon, A., Fellgett, M. W., & Williams, J. D. O. (2016). Use of borehole imaging to improve understanding of the in-situ stress orientation of Central and Northern England and its implications for unconventional hydrocarbon resources. *Marine and Petroleum Geology*, 73, 1–20. <https://doi.org/10.1016/j.marpetgeo.2016.02.012>

- Kulander, B. R., Dean, S. L., & Ward, B. J., Jr. (1990). *Fractured Core Analysis: Interpretation, Logging, and Use of Natural and Induced Fractures in Core* (Vol. 8). American Association of Petroleum Geologists.
- Langridge, R. M., Ries, W. F., Litchfield, N. J., Villamor, P., Van Dissen, R. J., Barrell, D. J. A., et al. (2016). The New Zealand active faults database. *New Zealand Journal of Geology and Geophysics*, 59(1), 86–96. <https://doi.org/10.1080/00288306.2015.1112818>
- Lawrence, M. J. F. (2018). Structural and sedimentological interpretation of well data from the wairoa area, North Island, New Zealand. GNS Science Report 2018/28. <https://doi.org/10.21420/G23W81.176>
- Li, D., McGuire, J. J., Liu, Y., & Hardebeck, J. L. (2018). Stress rotation across the Cascadia megathrust requires a weak subduction plate boundary at seismogenic depths. *Earth and Planetary Science Letters*, 485, 55–64. <https://doi.org/10.1016/j.epsl.2018.01.002>
- Li, Y., & Schmitt, D. R. (1998). Drilling-induced core fractures and in situ stress. *Journal of Geophysical Research*, 103(B3), 5225–5239. <https://doi.org/10.1029/97jb02333>
- Lin, W., Byrne, T. B., Kinoshita, M., McNeill, L. C., Chang, C., Lewis, J. C., et al. (2016). Distribution of stress state in the Nankai subduction zone, southwest Japan and a comparison with Japan Trench. *Tectonophysics*, 692, 120–130. <https://doi.org/10.1016/j.tecto.2015.05.008>
- Lin, W., Conin, M., Moore, J. C., Chester, F. M., Nakamura, Y., Mori, J. J., et al. (2013). Stress state in the largest displacement area of the 2011 Tohoku-Oki earthquake. *Science*, 339(687), 690. <https://doi.org/10.1126/science.1229379>
- Lin, W., Doan, M. L., Moore, J. C., McNeill, L., Byrne, T. B., Ito, T., et al. (2010). Present-day principal horizontal stress orientations in the Kumano forearc basin of the southwest Japan subduction zone determined from IODP NanTroSEIZE drilling Site C0009. *Geophysical Research Letters*, 37(13), 1–6. <https://doi.org/10.1029/2010GL043158>
- Litchfield, N. J., Van Dissen, R., Sutherland, R., Barnes, P. M., Cox, S. C., Norris, R., et al. (2014). A model of active faulting in New Zealand. *New Zealand Journal of Geology and Geophysics*, 57(1), 32–56. <https://doi.org/10.1080/00288306.2013.854256>
- Little, T. A., & Roberts, A. P. (1997). Distribution and mechanism of Neogene to present-day vertical axis rotations, Pacific-Australian plate boundary. *Journal of Geophysical Research*, 102(B9), 20447–20468. <https://doi.org/10.1029/97jb01279>
- Ma, K. F., Chan, C. H., & Stein, R. S. (2005). Response of seismicity to Coulomb stress triggers and shadows of the 1999 Mw = 7.6 Chi-Chi, Taiwan, earthquake. *Journal of Geophysical Research*, 110, B05S19. <https://doi.org/10.1029/2004JB003389>
- Magee, M. E., & Zoback, M. D. (1993). Evidence for a weak interplate thrust fault along the northern Japan subduction zone and implications for the mechanics of thrust faulting and fluid expulsion. *Geology*, 21(9), 809–812. [https://doi.org/10.1130/0091-7613\(1993\)021<0809:efawit>2.3.co;2](https://doi.org/10.1130/0091-7613(1993)021<0809:efawit>2.3.co;2)
- Malinverno, A., Saito, S., & Vannucchi, P. (2016). Horizontal principal stress orientation in the Costa Rica Seismogenesis Project (CRISP) transect from borehole breakouts. *Geochemistry, Geophysics, Geosystems*, 17(1), 65–77. <https://doi.org/10.1029/2015GC006092>
- McNamara, D. D., Behboudi, E., Wallace, L., Saffer, D. M., Cook, A. E., Fagereng, A., et al. (2021). Variable in-situ stress orientations across the northern Hikurangi Subduction Margin. *Geophysical Research Letters*, 48(5), e2020GL091707. <https://doi.org/10.1029/2020GL091707>
- Mochizuki, K., Sutherland, R., Henrys, S., Bassett, D., Van Avendonk, H., Arai, R., et al. (2019). Recycling of depleted continental mantle by subduction and plumes at the Hikurangi Plateau large igneous province, southwestern Pacific Ocean. *Geology*, 47(8), 795–798. <https://doi.org/10.1130/G46250.1>
- Mountjoy, J. J., & Barnes, P. M. (2011). Active upper plate thrust faulting in regions of low plate interface coupling, repeated slow slip events, and coastal uplift: Example from the Hikurangi Margin, New Zealand. *Geochemistry*, 12(1), Q01005. <https://doi.org/10.1029/2010gc003326>
- Nicol, A., & Beavan, J. (2003). Shortening of an overriding plate and its implications for slip on a subduction thrust, central Hikurangi Margin. *New Zealand Tectonics*, 22(6), 1070. <https://doi.org/10.1029/2003TC001521>
- Nicol, A., Mazengarb, C., Chanier, F., Rait, G., Uruski, C., & Wallace, L. (2007). Tectonic evolution of the active Hikurangi Subduction Margin, New Zealand, since the Oligocene. *Tectonics*, 26(4), 1–24. <https://doi.org/10.1029/2006TC002090>
- Pastori, M., Bacchesci, P., & Margheriti, L. (2019). Shear wave splitting evidence and relations with stress field and major faults from the “Amatrice-Visso-Nocria Sequence”. *Tectonics*, 38, 3351–3372. <https://doi.org/10.1029/2018TC005478>
- Pedley, K. L., Barnes, P. M., Pettinga, J. R., & Lewis, K. B. (2010). Seafloor structural geomorphic evolution of the accretionary frontal wedge in response to seamount subduction, Poverty Indentation, New Zealand. *Marine Geology*, 270(1–4), 119–138. <https://doi.org/10.1016/j.margeo.2009.11.006>
- Peška, P., & Zoback, M. D. (1995). Compressive and tensile failure of inclined well bores and determination of in situ stress and rock strength. *Journal of Geophysical Research*, 100(B7), 12791–12811. <https://doi.org/10.1029/95jb00319>
- Provost, A. S., & Houston, H. (2001). Orientation of the stress field surrounding the creeping section of the San Andreas Fault: Evidence for a narrow mechanically weak fault zone. *Journal of Geophysical Research*, 106(B6), 11373–11386. <https://doi.org/10.1029/2001JB900007>
- Rajabi, M., Tingay, M., & Heidbach, O. (2016a). The present-day state of tectonic stress in the Darling Basin, Australia: Implications for exploration and production. *Marine and Petroleum Geology*, 77, 776–790. <https://doi.org/10.1016/j.marpetgeo.2016.07.021>
- Rajabi, M., Tingay, M., & Heidbach, O. (2016b). The present-day stress field of New South Wales, Australia. *Australian Journal of Earth Sciences*, 63(1), 1–21. <https://doi.org/10.1080/08120099.2016.1135821>
- Reinecker, J., Tingay, M. R. P., & Müller, B. B. (2016). Borehole breakout analysis from four-arm caliper logs. In O. Heidbach, A. Barth, B. Müller, J. Reinecker, O. Stephansson, M. Tingay, & A. Zang (Eds.), *WSM quality ranking scheme, database description and analysis guidelines for stress indicator*. World Stress Map Technical Report 16-01. GFZ German Research Centre for Geosciences. <https://doi.org/10.2312/wsm.2016.001>
- Rice, J. R. (1992). Fault stress states, pore pressure distributions, and the weakness of the San Andreas fault. In *International Geophysics*, (Vol. 51, pp. 475–503). Academic Press. [https://doi.org/10.1016/S0074-6142\(08\)62835-1](https://doi.org/10.1016/S0074-6142(08)62835-1)
- Ruh, J. B., Sallarès, V., Ranero, C. R., & Gérya, T. (2016). Crustal deformation dynamics and stress evolution during seamount subduction: High-resolution 3-D numerical modeling. *Journal of Geophysical Research: Solid Earth*, 121, 6880–6902. <https://doi.org/10.1002/2016JB013250>
- Saffer, D. M., Flemings, B. P., Boutt, D., Doan, M.-L., Ito, T., McNeill, L., et al. (2013). In situ stress and pore pressure in the Kumano Forearc Basin offshore SW Honshu from downhole measurements during riser drilling. *Geochemistry, Geophysics, Geosystems*, 14(5), 1454–1470. <https://doi.org/10.1002/ggge.20051>
- Schellart, W. P., & Rawlinson, N. (2013). Global correlations between maximum magnitudes of subduction zone interface thrust earthquakes and physical parameters of subduction zones. *Physics of the Earth and Planetary Interiors*, 225, 41–67. <https://doi.org/10.1016/j.pepi.2013.10.001>
- Seeber, L., & Armbruster, J. G. (2000). Earthquakes as beacons of stress change. *Nature*, 407(6800), 69–72. <https://doi.org/10.1038/35024055>
- Sibson, R. H., & Rowland, J. V. (2003). Stress, fluid pressure and structural permeability in seismogenic crust, North Island, New Zealand. *Geophysical Journal International*, 154(2), 584–594. <https://doi.org/10.1046/j.1365-246x.2003.01965.x>
- Stein, R. S. (1999). The role of stress transfer in earthquake occurrence. *Nature*, 402(6762), 605–609. <https://doi.org/10.1038/45144>
- Sun, T., Saffer, D., & Ellis, S. (2020). Mechanical and hydrological effects of seamount subduction on megathrust stress and slip. *Nature Geoscience*, 13, 249–255. <https://doi.org/10.1038/s41561-020-0542-0>
- Tingay, M. R. P., Reinecker, J., & Müller, B. B. (2016). Borehole breakout and drilling-induced fracture analysis from image logs. In O. Heidbach, A. Barth, B. Müller, J. Reinecker, O. Stephansson, M. Tingay, & A. Zang (Eds.), *WSM quality ranking scheme, database description and analysis guidelines for stress indicator*. World Stress Map Technical Report 16-01. GFZ German Research Centre for Geosciences. <https://doi.org/10.2312/wsm.2016.001>

- analysis guidelines for stress indicator. World Stress Map Technical Report 16-01. GFZ German Research Centre for Geosciences. <https://doi.org/10.2312/wsm.2016.001>
- Tobin, H., Kinoshita, M., Ashi, J., Lallemand, S., Kimura, G., Scraton, E., et al. (2009). NanTroSEIZE Stage I expeditions : Introduction and synthesis of key results. In *Proceedings of the Integrated ocean drilling Program 314/315/31*. <https://doi.org/10.2204/iodp.proc.31431531.101.2009>
- Townend, J., Sherburn, S., Arnold, R., Boese, C., & Woods, L. (2012). Three-dimensional variations in present-day tectonic stress along the Australia-Pacific plate boundary in New Zealand. *Earth and Planetary Science Letters*, 353–354, 47–59. <https://doi.org/10.1016/j.epsl.2012.08.003>
- Townend, J., & Zoback, M. D. (2006). Stress, strain, and mountain building in central Japan. *Journal of Geophysical Research*, 111(3), 1–11. <https://doi.org/10.1029/2005JB003759>
- Vavryčuk, V. (2015). Earthquake Mechanisms and Stress Field. In M. Beer, I. Kougioumtzoglou, E. Patelli, & I. K. Au (Eds.), *Encyclopedia of earthquake engineering*. Springer. https://doi.org/10.1007/978-3-642-36197-5_295-1
- Wallace, L. M. (2020). Slow slip events in New Zealand. *Annual Review of Earth and Planetary Sciences*, 48(1), 175–203. <https://doi.org/10.1146/annurev-earth-071719-055104>
- Wallace, L. M., & Beavan, J. (2010). Diverse slow slip behavior at the Hikurangi Subduction Margin, New Zealand. *Journal of Geophysical Research*, 115(12), 1–20. <https://doi.org/10.1029/2010JB007717>
- Wallace, L. M., Beavan, J., Bannister, S., & Williams, C. (2012). Simultaneous long-term and short-term slow slip events at the Hikurangi Subduction Margin, New Zealand: Implications for processes that control slow slip event occurrence, duration, and migration. *Journal of Geophysical Research*, 117(B11), B11402. <https://doi.org/10.1029/2012JB009489>
- Wallace, L. M., Beavan, J., McCaffrey, R., & Darby, D. (2004). Subduction zone coupling and tectonic block rotations in the North Island. *New Zealand Journal of Geophysical Research*, 109(12), 1–21. <https://doi.org/10.1029/2004JB003241>
- Wallace, L. M., & Eberhart-Phillips, D. (2013). Newly observed, deep slow slip events at the central Hikurangi margin, New Zealand: Implications for downdip variability of slow slip and tremor, and relationship to seismic structure. *Geophysical Research Letters*, 40(20), 5393–5398. <https://doi.org/10.1002/2013GL057682>
- Wallace, L. M., Fagereng, Å., & Ellis, S. (2012). Upper plate tectonic stress state may influence interseismic coupling on subduction megathrusts. *Geology*, 40(10), 895–898. <https://doi.org/10.1130/G33373.1>
- Wang, K. (2000). Stress – Strain ‘paradox’, plate coupling, and forearc seismicity at the Cascadia and Nankai subduction zones. *Tectonophysics*, 319(4), 321–338. [https://doi.org/10.1016/s0040-1951\(99\)00301-7](https://doi.org/10.1016/s0040-1951(99)00301-7)
- Wang, K., Mulder, T., Rogers, G. C., & Hyndman, R. D. (1995). Case for very low coupling stress on the Cascadia subduction fault. *Journal of Geophysical Research*, 100(B7), 12907–12918. <https://doi.org/10.1029/95jb00516>
- Warren-Smith, E., Fry, B., Wallace, L. M., Chon, E., Henrys, S., Sheehan, A., et al. (2019). Episodic stress and fluid pressure cycling in subducting oceanic crust during slow slip. *Nature Geoscience*, 12(6), 475–481. <https://doi.org/10.1038/s41561-019-0367-x>
- Wenning, Q. C., Berthet, T., Ask, M., Zappone, A., Rosberg, J. E., & Almqvist, B. S. G. (2017). Image log analysis of in situ stress orientation, breakout growth, and natural geologic structures to 2.5 km depth in central Scandinavian Caledonides: Results from the COSC-1 borehole. *Journal of Geophysical Research: Solid Earth*, 122(5), 3999–4019. <https://doi.org/10.1002/2016JB013776>
- Williams, C. A., Eberhart-Phillips, D., Bannister, S., Barker, D. H. N., Henrys, S., Reyners, M., & Sutherland, R. (2013). Revised interface geometry for the Hikurangi subduction zone. *New Zealand Seismological Research Letters*, 84(6), 1066–1073. <https://doi.org/10.1785/0220130035>
- Wu, H., Kinoshita, M., & Sanada, Y. (2012). Stress state estimation by geophysical log in NanTroSEIZE Expedition 319-Site C0009, Kumano Basin, southwest Japan. *Geophysical Research Letters*, 39, L18303. <https://doi.org/10.1029/2012GL053086>
- Yang, Z., Sheehan, A., & Shearer, P. (2011). Stress - induced upper crustal anisotropy in southern California. *Journal of Geophysical Research*, 116(B2), B02302. <https://doi.org/10.1029/2010JB007655>
- Zinke, J. C., & Zoback, M. D. (2000). Structure-related and stress-induced shear-wave velocity anisotropy: Observations from microearthquakes near the Calaveras fault in central California. *Bulletin of the Seismological Society of America*, 90(5), 1305–1312. <https://doi.org/10.1785/0119990099>
- Zoback, M. D. (2007). *Reservoir geomechanics*. Cambridge University Press.
- Zoback, M. D., Zoback, M. L., Eaton, J. P., Mount, V. S., Suppe, J., Healy, J. H., et al. (1987). New evidence on the state of stress of the San Andreas Fault. *Science*, 238, 1105–1111. <https://doi.org/10.1126/science.238.4830.1105>

Reference From the Supporting Information

- Hillis, R. R., & Reynolds, S. D. (2003). In situ stress field of Australia. *Geological Society of America Special Papers*, 372, 49–58. <https://doi.org/10.1130/0-8137-2372-8.49>